The Astrophysical Journal, 927:61 (17pp), 2022 March 1 https://doi.org/10.3847/1538-4357/ac4bb9

Investigating the Observational Properties of Type Ib Supernova SN 2017iro

Brajesh Kumar[1,2], Avinash Singh[2,3], D. K. Sahu[2], and G. C. Anupama[2]
[1] Aryabhatta Research Institute of Observational Sciences, Manora Peak, Nainital—263001, India; brajesh@aries.res.in, brajesharies@gmail.com
[2] Indian Institute of Astrophysics, II Block, Koramangala, Bengaluru 560034, India
[3] Hiroshima Astrophysical Science Center, Hiroshima University, Higashi-Hiroshima, Hiroshima 739-8526, Japan
Received 2021 October 18; revised 2021 December 29; accepted 2022 January 9; published 2022 March 4

Abstract

We report results of optical imaging and low-resolution spectroscopic monitoring of supernova (SN) 2017iro that occurred in the nearby (∼31 Mpc) galaxy NGC 5480. The He I λ5876 feature present in the earliest spectrum (−7 days) classified it as a Type Ib SN. The follow-up observations span from −7 to +266 days with respect to the *B*-band maximum. With a peak absolute magnitude in *V* band $M_V = -17.76 \pm 0.15$ mag and bolometric luminosity $\log_{10} L = 42.39 \pm 0.09$ erg s^{-1}, SN 2017iro is a moderately luminous Type Ib SN. The overall light-curve evolution of SN 2017iro is similar to that of SN 2012au and SN 2009jf during the early (up to ∼100 days) and late phases (>150 days), respectively. The line velocities of both Fe II λ5169 and He I λ5876 are ∼9000 km s^{-1} near the peak. The analysis of the nebular phase spectrum (∼+209 days) indicates an oxygen mass of ∼0.35 $M_\odot$. The smaller [O I]/[Ca II] flux ratio of ∼1 favors a progenitor with a zero-age main-sequence mass in the range ∼13–15 $M_\odot$, most likely in a binary system, similar to the case of iPTF13bvn. The explosion parameters are estimated by applying different analytical models to the quasi-bolometric light curve of SN 2017iro. ^{56}Ni mass synthesized in the explosion has a range of ∼0.05–0.10 $M_\odot$, ejecta mass ∼1.4–4.3 $M_\odot$, and kinetic energy $\sim(0.8–1.9) \times 10^{51}$ erg.

Unified Astronomy Thesaurus concepts: Type Ib supernovae (1729); Supernovae (1668); Core-collapse supernovae (304)

Supporting material: data behind figure

1. Introduction

Type Ib, Ic, Ic broad-lined (Ic-BL), and IIb supernovae (SNe) belong to the class of stripped-envelope SNe (SE-SNe; Minkowski 1941; Clocchiatti & Wheeler 1997; Filippenko 1997; Gal-Yam 2017, p. 195; Modjaz et al. 2019). SE-SNe are generally characterized by bell-shaped light curves (LCs) that are mainly powered by the thermal energy released as a consequence of radioactive decay of the iron-group elements (^{56}Ni → ^{56}Co → ^{56}Fe) synthesized in the explosion. SE-SNe show no hydrogen (Ib) or neither hydrogen nor helium (Ic) in their spectra except for Type IIb events, which exhibit hydrogen in the early-phase spectra (Filippenko 1988; Filippenko et al. 1993). This indicates that they are the results of explosion of stars that are devoid of the outer layer of hydrogen (Ib) or both hydrogen and helium (Ic) at the time of explosion. The spectroscopic behavior of SE-SNe separates them from Type II SNe, where hydrogen is found to be dominant in the spectra. The SE-SNe and Type II events are collectively grouped as core-collapse SNe (CCSNe), as they result from the gravitational collapse of the iron core of massive stars ($M \geqslant 8\,M_\odot$) during the end stages of their lives (Heger et al. 2003; Smartt 2009).

In SE-SNe, the mechanisms responsible for removing the outer envelopes (hydrogen or helium) of the progenitors can be radiation-driven stellar winds (Conti 1975; Puls et al. 2008; Pauldrach et al. 2012), eruptive mass loss (Smith 2006; Smith & Owocki 2006), and/or mass transfer to a companion star (Nomoto 1984, 1987; Wheeler & Levreault 1985; Podsiadlowski et al. 1992; Nomoto et al. 1995; Woosley & Weaver 1995; Wellstein & Langer 1999; Wellstein et al. 2001; Pols & Dewi 2002; Podsiadlowski et al. 2004; Yoon et al. 2010). Depending on the main-sequence mass of the progenitor star, the above mechanisms or a combination of them operate. In the case of a single massive (>20 $M_\odot$) Wolf-Rayet star, the radiation-driven stellar wind is the dominant process (see Woosley et al. 1995; Massey 2003; Crowther 2007; Smith 2014; Yoon 2015, and references therein). In the case of moderately massive (8–25 $M_\odot$) stars, mass transfer to the binary companion effectively removes the outer envelope (Groh et al. 2013; Smith 2014; Yoon 2015, and references therein).

Dedicated and large-area transient survey programs have made it possible to discover a large number of SNe of different types. The SE-SNe constitute a reasonable fraction (∼25%–30%) of the overall SN rate in the local universe (Li et al. 2011; Eldridge et al. 2013; Graur et al. 2017a, 2017b). The availability of ample data has led to a qualitative analysis of a large sample of SE-SNe in recent years (see, e.g., Drout et al. 2011; Bianco et al. 2014; Modjaz et al. 2014; Taddia et al. 2015; Liu et al. 2016; Lyman et al. 2016; Prentice et al. 2016; Taddia et al. 2018; Prentice et al. 2019; Shivvers et al. 2019; Williamson et al. 2019; Shahbandeh et al. 2022). These studies reveal that heterogeneity exists in the observational properties of SE-SNe in terms of synthesized ^{56}Ni masses (∼0.1–0.4 $M_\odot$), ejecta masses (∼1–6 $M_\odot$), explosion energies (few × 10^{51} erg), and absolute magnitude (∼−17 to −18 mag). Notably, the sample selection criteria and the methods applied may induce inconsistency in various estimates (see Taddia et al. 2018; Prentice et al. 2019).

Statistical investigations of a large sample of photometric data are useful in exploring the bulk properties of various types of events. Nevertheless, such studies are generally limited to LCs in selected passbands, and also the follow-up covers a short duration

of the SN evolution. Further, the spectroscopic follow-up of most objects is restricted to early phases. Nonuniformity in the data sample may also be present, as these are collected at different observing facilities and detectors. Studying individual events with proper monitoring at different phases (both photospheric and nebular) is hence extremely important. The very early phase observations (hours to days after explosion) of these events are useful to constrain the progenitor radius at its end stage. This needs a very early detection and quick follow-up, which is not always possible considering their random occurrence in the sky. The large-area surveys with high cadence have contributed significantly in this regard. SN 1993J (Type IIb) is the first event among SE-SNe that shows evidence of a prominent cooling tail just after explosion (Richmond et al. 1994; Barbon et al. 1995). During the past two decades, several Type IIb SNe with such interesting features have been monitored and studied well, e.g., SN 2008ax (Pastorello et al. 2008; Roming et al. 2009), SN 2011dh (Arcavi et al. 2011), SN 2011fu (Kumar et al. 2013; Morales-Garoffolo et al. 2015), SN 2013df (Fremling et al. 2014), and SN 2016gkg (Arcavi et al. 2017; Tartaglia et al. 2017). A handful of Type Ib events have also been discovered at very early phases, such as SN 1999ex (Hamuy et al. 2002; Stritzinger et al. 2002), SN 2008D (Mazzali et al. 2008; Soderberg et al. 2008; Malesani et al. 2009; Modjaz et al. 2009; Bersten et al. 2013), iPTF13bvn (Bersten et al. 2014; Fremling et al. 2016), and LSQ13abf (Stritzinger et al. 2020), and their observational properties are studied in detail. Recently, Prentice et al. (2019) analyzed the properties of 18 SE-SNe and discussed the implications for their progenitors. Direct detection of SE-SNe progenitor candidates has been possible only for a few objects, e.g., SN 1993J (Maund et al. 2004), SN 2011dh (Maund et al. 2011; Van Dyk et al. 2013), SN 2001ig (Ryder et al. 2018), iPTF13bvn (Cao et al. 2013; Eldridge et al. 2015; Kuncarayakti et al. 2015; Folatelli et al. 2016), SN 2016gkg (Kilpatrick et al. 2017; Tartaglia et al. 2017), SN 2017ein (Kilpatrick et al. 2018; Van Dyk et al. 2018; Xiang et al. 2019), and SN 2019yvr (Kilpatrick et al. 2021). Along with very early phases, the temporal observations during maximum to nebular phases are equally important to estimate various explosion parameters and progenitor properties. Detailed investigation of more events can provide an alternative way to understand various progenitor channels.

SN 2017iro was discovered by Patrick Wiggins on 2017 November 30.5 UT (Wiggins 2017) at about 15″ southeast of the center of the galaxy NGC 5480, which also hosted another Type Ib event SN 1988L (Perlmutter et al. 1988). Pre-explosion images of the host galaxy, obtained by the Hubble Space Telescope (HST) in the F606W band using the Wide Field Camera (WFC) of the Advanced Camera for Surveys (ACS), exist in the HST archive. SN 2017iro was discovered at a magnitude of ∼15.5 mag (clear filter) and classified as a Type Ib/c SN with the help of the spectrum taken on 2017 December 2 (Bertrand 2017). Noting that SN 2017iro discovery was slightly late (∼8 days after explosion), however, we were able to cover its peak and the late-phase observations with a good sampling of photometric and spectroscopic data points. Table 1 lists details of SN 2017iro and its host galaxy.

Results based on well-sampled optical photometric and low-resolution spectroscopic observations of SN 2017iro are presented in this paper. The observations and data reduction are described in Section 2. LC and spectral properties are presented in Sections 3 and 4, respectively. In Section 5, the results are discussed, and the summary is provided in Section 6.

Table 1
Details of SN 2017iro and Its Host Galaxy

Parameters	Value	Reference
SN 2017iro:		
R.A. (J2000)	$14^{h}\,06^{m}\,23\overset{s}{.}11$	1
Decl. (J2000)	$+50°\,43'\,20\overset{''}{.}20$	1
Explosion epoch (UT)	2017 November 23 (JD 2,458,080.7)	Section 3.1
Discovery date (UT)	2017 November 30.5 (JD 2,458,088.0)	1
$E(B-V)_{\rm total}$	0.28 ± 0.04 mag	Section 3.3
NGC 5480:		
Type	SA(s)c	2
Redshift	0.006191 ± 0.000017	2
Distance	30.8 ± 2.2 Mpc	3
Distance modulus	32.44 ± 0.15 mag	3

Note. (1) https://wis-tns.weizmann.ac.il/object/2017iro; (2) NASA/IPAC Extragalactic Database (NED); (3) Mould et al. (2000).

2. Observations and Data Reduction

2.1. Photometric Observation

The photometric follow-up of SN 2017iro started just after the announcement of its discovery, i.e., 2017 December 1 (JD 2,458,089.5), and continued up to 2018 August 31 (JD 2,458,362.1). These observations were performed in Bessell *UBVRI* bands with the Himalayan Faint Object Spectrograph Camera (HFOSC), mounted on the $f/9$ Cassegrain focus of the 2 m Himalayan Chandra Telescope (HCT) of Indian Astronomical Observatory (IAO), Hanle, India (Prabhu 2014). HFOSC is equipped with a liquid-nitrogen-cooled 2k × 4k pixel SITe CCD chip (pixel size 15 × 15 μm). The gain and readout noise of the detector are 1.22 e^{-}/ADU and 4.87 e^{-}, respectively. With a plate scale of $0\overset{''}{.}296$ pixel^{-1}, the central 2k × 2k region covers a field of $10' \times 10'$ on the sky and is used for imaging. Further description on the HCT and the HFOSC instrument can be obtained from https://www.iiap.res.in/?q=iao_about.

During the observations, several bias and twilight flat frames were obtained along with science frames. The usual pre-processing steps, such as bias subtraction, flat-fielding correction, and cosmic-ray removal, were applied to raw images of the SN. For this purpose, standard tasks available in the data reduction software IRAF[4] were used. In order to achieve a better signal-to-noise ratio, multiple frames were taken on some nights and co-added in respective bands after the alignment of the images.

To calibrate a sequence of secondary standards in the SN field, we observed Landolt photometric standard fields (Landolt 1992) PG 0231+051, PG 0918+029, PG 0942−029, and PG 1047+003 on three nights, 2018 January 21 and February 03 and 25, under good photometric conditions along with the SN field. The observed Landolt field stars cover a brightness range of $12.27 \text{ mag} \leqslant V \leqslant 16.11$ mag and color range of

[4] IRAF stands for Image Reduction and Analysis Facility. It is distributed by the National Optical Astronomy Observatory, which is operated by the Association of Universities for Research in Astronomy (AURA) under a cooperative agreement with the National Science Foundation.

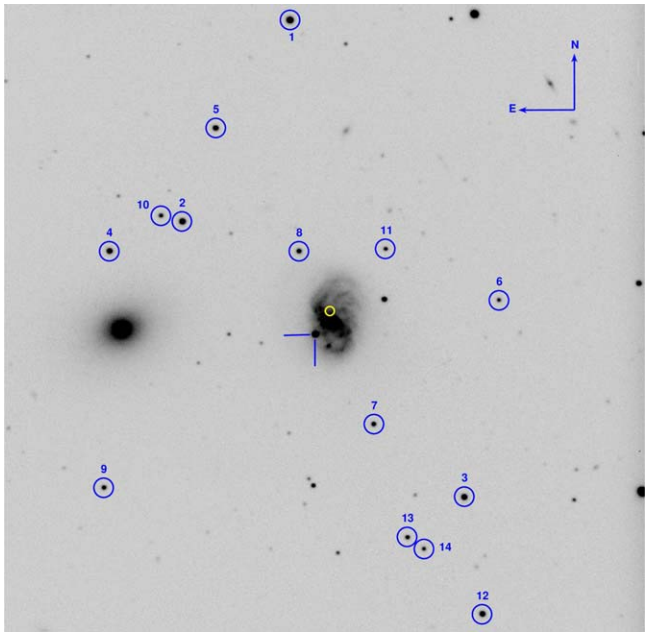

Figure 1. Identification chart of SN 2017iro obtained in *V* band (SN is marked with blue crosshairs). The field of view is roughly $9' \times 9'$. IDs 1–14 indicate secondary standard stars in the SN field (their magnitudes are listed in Table 2). The location of SN 1988L is also marked with a yellow circle.

-0.33 mag $\leqslant B - V \leqslant 1.45$ mag. The average atmospheric extinction values in *U*, *B*, *V*, *R*, and *I* bands for the site were adopted from Stalin et al. (2008). The average color terms for the telescope detector system were used to determine the photometric zero-points by applying a linear relationship between the observed and standard colors. A set of 14 stars in the SN field (marked in Figure 1) were calibrated using the estimated zero-points and average color terms. The calibrated *UBVRI* magnitudes of the secondary standards averaged over three nights are listed in Table 2. Considering the proximity of SN to an H II region, template subtraction was performed using the template images of the host galaxy, observed on 2019 August 21 with the HCT. The instrumental magnitudes of the SN at different epochs were extracted from the template-subtracted images. The SN magnitude is calibrated differentially with respect to the secondary standards in the SN field by applying the nightly zero-points (see Kumar et al. 2018). The photometric magnitudes of SN, along with the errors, are listed in Table 3. Here, photometric errors include the errors in aperture photometry as estimated in IRAF and uncertainties in the nightly zero-points, added in quadrature.

2.2. Spectroscopic Observation

Low-resolution optical spectroscopic observations of SN 2017iro were obtained at 34 epochs from 2017 December 01 (JD 2,458,089.4) to 2018 July 05 (JD 2,458,305.2). Two grisms Gr#7 (3500–7800 Å) and Gr#8 (5200–9250 Å), available with HFOSC, were used to obtain the SN 2017iro spectra. The spectra of arc lamp and spectrophotometric standards were obtained along with the SN for calibration purposes. The spectroscopic data reduction was carried out in a standard way using IRAF. After correcting the observed frames for bias and flat fields, one-dimensional spectra were extracted using the optimal extraction method. Wavelength calibration was done by applying the dispersion solutions obtained using arc lamp spectra. The night-sky emission lines were utilized to secure the wavelength calibration, and small shifts were applied wherever necessary. The spectrophotometric standard observed on the same night was used in obtaining the instrumental response curves for flux calibration of the spectra. For those nights where standard-star observations were not possible, the response curves obtained during nearby nights were used. To construct a single flux-calibrated spectrum, the spectra in both the grisms (Gr#7, Gr#8) were combined. The spectra were then scaled with respect to the calibrated *UBVRI* fluxes to bring them to an absolute flux scale. Finally, the SN spectra were corrected for the host galaxy redshift of $z = 0.006191$ (from NED).

3. Photometric Evolution

3.1. Estimation of Explosion Epoch and Optical Light Curves

The last nondetection of SN 2017iro was reported (Wiggins 2017) on 2017 November 15.1 (JD 2,458,072.6) with a limiting magnitude of 19 mag. However, the SN was discovered on 2017 November 30.5 (JD 2,458,088.0). Since there is a large gap between the first detection and last nondetection, various approaches were considered for estimating the explosion epoch. The explosion epoch was estimated by fitting a power law of the form $L(t) = A \times (t - t_0)^{0.78}$ (Piro & Nakar 2013) to the pre-maximum phase of the LC. Here L denotes the luminosity at time t, A is a constant that defines the rising rate, and t_0 is the time of the explosion. The best-fit value of t_0 is computed as JD 2,458,077.1 (2017 November 21.1). While evaluating the explosion parameters of SN 2017iro (see Section 3.4), the model of Valenti et al. (2008) was best fitted for an explosion date of JD 2,458,084.0 (2017 November 26.5). An analytical function (Taddia et al. 2018) fitted to the LC (see Section 3.2) yielded an explosion epoch of JD 2,458,080.0 (2017 November 22.5). An average of the above values, i.e., JD 2,458,080.4 ± 2.0 (2017 November 22.9), was adopted as the explosion epoch of SN 2017iro (see Table 4). Further, the typical rise times of Type Ib SNe in *R* band and bolometric LCs are ∼22 days (Taddia et al. 2015) and ∼17 days (Lyman et al. 2016), respectively. The *R*-band and the bolometric peak of SN 2017iro occurred on JD 2,458,099.4 and JD 2,458,096.6, respectively (see Section 3.2). The mean explosion date estimated above is consistent with the rise time criteria.

The *UBVRI* LCs of SN 2017iro are shown in Figure 2 (left panel). A well-sampled LC covering the pre-maximum to nebular phase was obtained using the photometric observation made on 40 epochs. In the right panel of Figure 2, the *V*-band LCs of well-studied Type Ib SNe, iPTF13bvn (Srivastav et al. 2014; Kuncarayakti et al. 2015), SN 2012au (Pandey et al. 2021), SN 2009jf (Sahu et al. 2011; Valenti et al. 2011), SN 2007Y (Stritzinger et al. 2009), and SN 1999dn (Benetti et al. 2011), having observations during pre-maximum and nebular phases, are plotted along with SN 2017iro for comparison. The LC evolution and estimation of related parameters are discussed in the following subsections.

3.2. Light-curve Parameters

Various LC parameters were obtained by fitting the LCs in different bands with an analytical function proposed by Taddia et al. (2018, see their Section 3). This method is based on the empirical model suggested by Vacca & Leibundgut (1996) for thermonuclear events, whose LCs are similar to those of

Table 2
Calibrated Magnitudes of Secondary Standards in the Field of SN 2017iro

Star ID	U (mag)	B (mag)	V (mag)	R (mag)	I (mag)
1	15.86 ± 0.07	15.93 ± 0.02	15.34 ± 0.01	14.95 ± 0.02	14.56 ± 0.01
2	16.16 ± 0.06	16.39 ± 0.01	15.87 ± 0.01	15.53 ± 0.02	15.20 ± 0.01
3	18.02 ± 0.02	17.21 ± 0.02	16.21 ± 0.01	15.59 ± 0.01	15.07 ± 0.01
4	18.09 ± 0.09	17.26 ± 0.01	16.22 ± 0.01	15.57 ± 0.02	15.00 ± 0.01
5	17.21 ± 0.06	17.10 ± 0.01	16.41 ± 0.01	15.97 ± 0.02	15.54 ± 0.01
6	19.83 ± 0.05	19.33 ± 0.05	17.85 ± 0.02	16.50 ± 0.02	14.91 ± 0.02
7	17.62 ± 0.01	17.74 ± 0.01	17.14 ± 0.01	16.76 ± 0.02	16.41 ± 0.02
8	17.33 ± 0.04	17.51 ± 0.02	16.95 ± 0.02	16.59 ± 0.03	16.24 ± 0.03
9	18.14 ± 0.02	17.96 ± 0.01	17.23 ± 0.01	16.78 ± 0.02	16.38 ± 0.01
10	19.92 ± 0.69	18.90 ± 0.04	17.48 ± 0.02	16.30 ± 0.02	14.92 ± 0.01
11	18.27 ± 0.01	18.33 ± 0.02	17.68 ± 0.02	17.28 ± 0.02	16.84 ± 0.06
12	18.17 ± 0.05	17.36 ± 0.01	16.40 ± 0.01	15.80 ± 0.02	15.29 ± 0.01
13	18.04 ± 0.01	18.11 ± 0.01	17.51 ± 0.01	17.12 ± 0.02	16.74 ± 0.01
14	18.66 ± 0.02	18.52 ± 0.02	17.80 ± 0.02	17.36 ± 0.03	16.95 ± 0.03

Note. Star IDs are indicated in Figure 1.

SE-SNe. The epoch of maximum and the LC parameters of SN 2017iro estimated from the LCs of different passbands are listed in Table 5 and are compared with other SE-SNe. A lag of ∼5 days between U- and I-band maximum is inferred for SN 2017iro. This duration is shorter in comparison to ∼8 days for the slow-declining SN 2009jf (Sahu et al. 2011) and ∼9 days for the fast-declining iPTF13bvn (Srivastav et al. 2014). The early appearance of maximum in bluer bands is a common behavior of SE-SNe, and SN 2017iro follows this trend.

The luminosity decline rate parameter, Δm_{15} (difference in magnitude at peak and 15 days later), is handy in the context of Type Ia SNe, where it is found to be correlated with the peak luminosity. A smaller Δm_{15} value favors more luminous objects (Phillips 1993). Large data sets obtained from different surveys have provided an opportunity to investigate whether such a correlation exists for SE-SNe. No direct correlation was found between the LC decline rate parameter and luminosity by Drout et al. (2011) and Taddia et al. (2015). However, the sample study of a larger set of SE-SNe in Taddia et al. (2018) hinted toward the fact that luminous events tend to have broader LCs, i.e., a smaller value of Δm_{15}. In the following paragraph, we compared various LC parameters of SN 2017iro with some well-studied Type Ib SNe.

The Δm_{15} values of SN 2017iro are 1.46, 0.77, 0.69, and 0.52 mag in B, V, R, and I bands, respectively. These are similar to the values inferred for SN 2012au (Pandey et al. 2021; 1.60, 0.90, 0.70, and 0.43 mag, respectively). On the other hand, iPTF13bvn shows comparatively rapid evolution (1.82, 1.16, 1.22, and 0.90 mag, respectively; Srivastav et al. 2014), whereas SN 2009jf shows a relatively slower evolution (Sahu et al. 2011; 0.91, 0.50, 0.31, and 0.31 mag, respectively). The above can be inferred from the comparison of normalized V-band LCs shown in the right panel of Figure 2. The comparison of early-phase LCs indicates that the decline rate of SN 2017iro is intermediate between the fast-declining SN 2007Y and iPTF13bvn and the slow-declining SN 2009jf. The intermediate width of LCs of SN 2017iro could possibly indicate that ejecta mass of SN 2017iro lies in between the inferred ejecta mass of iPTF13bvn and SN 2009jf (see Section 5.3).

The decay in the magnitude from the peak to +40 days is denoted by the Δm_{40} parameter by Taddia et al. (2018). Δm_{40} was found to be in the range of 1.5−1.7 mag (in r band) for their sample of SE-SNe. SN 2017iro lies toward the lower end (1.54 mag in R-band) of the observed range, indicating a relatively faster evolution for an SE-SN. The late-phase (>40 days) LC decay rate of SN 2017iro is also computed in all bands (see Table 5). The decay rates between ∼+40 and ∼+140 days are 1.27, 1.73, 1.57, and 1.75 mag 100 day^{-1} (in B, V, R, and I bands, respectively) and beyond ∼140 days are 1.80, 1.52, and 1.90 mag 100 day^{-1} (in V, R, and I bands, respectively). It is to be noted that usually SE-SNe display faster decline than Type II events during the late phases. Such features are indicative of higher γ-ray escape. The implications of the fast-declining nature of SN 2017iro are discussed in Section 5.1.

The V-band absolute magnitude (M_V) of SE-SNe is known to display a wide range between ∼−16.5 and ∼−19.5 mag (Richardson et al. 2006; Drout et al. 2011; Taddia et al. 2018). To estimate the M_V of SN 2017iro, we adopted the distance of the host galaxy NGC 5480 as 30.8 ± 2.2 Mpc (corrected for Virgo infall only) and the corresponding distance modulus 32.44 ± 0.15 mag (for an $H_0 = 73$ km s^{-1} Mpc^{-1}). The adopted distance is consistent with the distance estimate of 30.73 Mpc using the Tully–Fisher relation (Theureau et al. 2007). After applying a correction for the reddening $E(B-V) = 0.28$ mag (see Section 3.3), the M_V of SN 2017iro is derived as −17.76 ± 0.15 mag. This indicates that SN 2017iro is fainter than SN 2007uy, SN 2009jf, and SN 2012au but brighter than SN 2007Y and iPTF13bvn.

3.3. Reddening and Color Evolution

The estimate of reddening suffered by SN is crucial, as it affects the explosion parameters that are derived using the observables. The reddening due to ISM in the Milky Way along the line of sight (LOS) of the SN can be inferred using the all-sky dust extinction map (e.g., Schlafly & Finkbeiner 2011; Schlafly et al. 2016). The determination of reddening within the host galaxy is a challenging task. In general, the sites of SE-SNe are associated with star-forming regions (e.g., Anderson et al. 2012; Eldridge et al. 2013) and may suffer a considerable amount of reddening. Several photometric and spectroscopic techniques have been proposed to determine the reddening within the host galaxy but with caveats.

Table 3
Log of Photometric Observations and Estimated *UBVRI* Magnitudes of SN 2017iro

Date (yyyy-mm-dd)	JD 2,450,000+	Phase[a] (days)	*U* (mag)	*B* (mag)	*V* (mag)	*R* (mag)	*I* (mag)
2017 12 01	8089.5	−6.7	15.85 ± 0.11	16.29 ± 0.03	16.01 ± 0.11	15.78 ± 0.04	15.67 ± 0.07
2017 12 02	8090.5	−5.7	15.71 ± 0.11	16.20 ± 0.13	15.93 ± 0.11	15.71 ± 0.03	15.56 ± 0.08
2017 12 05	8093.4	−2.8	15.64 ± 0.11	15.96 ± 0.13	15.68 ± 0.05	15.47 ± 0.09	15.33 ± 0.11
2017 12 06	8094.4	−1.8	15.64 ± 0.11	16.01 ± 0.09	15.63 ± 0.11	15.38 ± 0.05	15.21 ± 0.07
2017 12 07	8095.5	−0.7	15.63 ± 0.12	15.95 ± 0.05	15.56 ± 0.03	15.25 ± 0.02	15.118 ± 0.03
2017 12 08	8096.5	+0.3	15.68 ± 0.12	15.92 ± 0.06	15.56 ± 0.10	15.22 ± 0.10	15.10 ± 0.13
2017 12 09	8097.5	+1.3	⋯	⋯	15.52 ± 0.02	15.20 ± 0.03	15.06 ± 0.03
2017 12 12	8100.5	+4.3	15.84 ± 0.12	16.12 ± 0.11	15.58 ± 0.01	15.19 ± 0.04	14.99 ± 0.06
2017 12 14	8102.5	+6.3	⋯	16.33 ± 0.05	15.69 ± 0.04	15.19 ± 0.02	14.96 ± 0.08
2017 12 17	8105.4	+9.2	17.00 ± 0.13	16.74 ± 0.03	15.84 ± 0.05	15.32 ± 0.02	15.06 ± 0.04
2017 12 26	8114.4	+18.2	18.50 ± 0.14	17.76 ± 0.04	16.43 ± 0.02	15.81 ± 0.04	15.38 ± 0.04
2017 12 29	8117.4	+21.2	⋯	⋯	16.61 ± 0.02	15.98 ± 0.02	15.59 ± 0.02
2018 01 05	8124.5	+28.3	⋯	18.28 ± 0.04	16.90 ± 0.06	16.27 ± 0.02	15.77 ± 0.07
2018 01 07	8126.4	+30.2	19.07 ± 0.14	⋯	16.96 ± 0.10	16.32 ± 0.08	15.84 ± 0.07
2018 01 08	8127.4	+31.2	⋯	⋯	16.96 ± 0.06	16.25 ± 0.11	15.79 ± 0.09
2018 01 14	8133.4	+37.2	⋯	18.40 ± 0.03	17.14 ± 0.01	16.51 ± 0.02	15.99 ± 0.03
2018 01 16	8135.4	+39.2	19.10 ± 0.20	18.50 ± 0.04	17.21 ± 0.02	16.57 ± 0.04	16.03 ± 0.06
2018 01 17	8136.5	+40.3	⋯	18.52 ± 0.06	17.24 ± 0.02	16.62 ± 0.02	16.05 ± 0.05
2018 01 21	8140.4	+44.2	⋯	18.49 ± 0.03	17.31 ± 0.02	16.72 ± 0.01	16.12 ± 0.05
2018 01 30	8149.3	+53.1	⋯	18.66 ± 0.02	17.40 ± 0.10	16.86 ± 0.10	16.19 ± 0.04
2018 02 02	8152.4	+56.2	⋯	18.57 ± 0.05	17.50 ± 0.05	16.94 ± 0.03	16.34 ± 0.04
2018 02 03	8153.3	+57.1	19.22 ± 0.21	18.61 ± 0.12	17.51 ± 0.07	16.94 ± 0.06	16.32 ± 0.07
2018 02 09	8159.4	+63.2	⋯	18.65 ± 0.02	17.63 ± 0.02	16.98 ± 0.02	16.41 ± 0.04
2018 02 13	8163.3	+67.1	19.08 ± 0.15	18.73 ± 0.03	17.69 ± 0.02	17.12 ± 0.03	16.50 ± 0.04
2018 02 16	8166.3	+70.1	19.14 ± 0.17	18.70 ± 0.07	17.76 ± 0.02	17.20 ± 0.03	16.57 ± 0.05
2018 02 20	8170.3	+74.1	⋯	18.77 ± 0.02	17.83 ± 0.01	17.28 ± 0.02	16.64 ± 0.04
2018 02 25	8175.2	+79.0	⋯	18.79 ± 0.11	17.90 ± 0.03	17.36 ± 0.03	16.72 ± 0.03
2018 03 07	8185.2	+89.0	⋯	18.96 ± 0.07	18.09 ± 0.02	17.53 ± 0.02	16.87 ± 0.05
2018 03 15	8193.3	+97.1	⋯	⋯	18.22 ± 0.01	17.69 ± 0.01	17.05 ± 0.02
2018 03 23	8201.4	+105.2	⋯	19.18 ± 0.02	18.35 ± 0.02	17.86 ± 0.02	17.19 ± 0.03
2018 03 30	8208.3	+112.1	⋯	⋯	18.47 ± 0.05	17.92 ± 0.04	17.30 ± 0.03
2018 04 02	8211.4	+115.2	⋯	19.28 ± 0.09	18.50 ± 0.05	18.02 ± 0.03	17.38 ± 0.05
2018 04 07	8216.3	+120.1	⋯	⋯	18.56 ± 0.02	17.99 ± 0.02	17.38 ± 0.02
2018 04 15	8224.3	+128.1	⋯	19.50 ± 0.02	18.71 ± 0.01	18.20 ± 0.01	17.60 ± 0.03
2018 04 21	8230.2	+134.0	⋯	19.64 ± 0.02	18.85 ± 0.03	18.30 ± 0.01	17.76 ± 0.02
2018 04 28	8237.4	+141.2	⋯	19.79 ± 0.17	18.98 ± 0.06	18.34 ± 0.04	17.86 ± 0.04
2018 05 01	8240.3	+144.1	⋯	⋯	19.03 ± 0.04	18.47 ± 0.03	17.88 ± 0.04
2018 05 30	8269.2	+173.0	⋯	⋯	⋯	18.83 ± 0.02	18.38 ± 0.04
2018 07 05	8305.2	+209.0	⋯	⋯	20.20 ± 0.03	19.41 ± 0.02	18.96 ± 0.03
2018 08 31	8362.1	+265.9	⋯	⋯	21.22 ± 0.14	20.28 ± 0.12	20.16 ± 0.15

Note.
[a] With reference to the *B*-band maximum (JD 2,458,096.2).

The Galactic reddening along the LOS of SN 2017iro as derived from the all-sky dust extinction map (Schlafly & Finkbeiner 2011) is $E(B-V) = 0.016 \pm 0.001$ mag. The equivalent width (EW) of Na I D absorption lines is considered as a good tracer of reddening within the host galaxy (Barbon et al. 1990; Turatto et al. 2003; Poznanski et al. 2012) but with caveats (Poznanski et al. 2011; Phillips et al. 2013). To estimate the EW of Na I D, we stacked the low-resolution spectra of SN 2017iro obtained near the maximum light. A reasonably strong Na I D absorption feature is seen at the redshift of the host galaxy with an EW $= 1.34 \pm 0.10$ Å. An average value of $E(B-V)_{\rm host}$, computed from the relation of Barbon et al. (1990) and Turatto et al. (2003), is 0.27 ± 0.04 mag. For further analysis we adopt a total extinction $E(B-V)_{\rm MW+host} = 0.28 \pm 0.04$ mag (Milky Way + host) and Cardelli et al. (1989) extinction law with ratio of selective to total extinction $R_V = 3.1$.

In Figure 3, the $B-V$, $V-R$, and $R-I$ colors of SN 2017iro are compared with other well-studied Type Ib events (see Table 6 for details and references). It is seen that the overall shape of color evolution for each color is similar (also see Stritzinger et al. 2018). Up to ∼+20 days, the $B-V$ color evolves faster than the $V-R$ and $R-I$ colors. During the late phase (>20 days), the color evolution is almost flat.

3.4. Quasi-bolometric Light Curve

The quasi-bolometric LC of SN 2017iro was constructed using the latest version of the Python-based code SUPERBOL (Nicholl 2018). The *UBVRI* magnitudes after correcting for the total extinction $E(B-V) = 0.28$ mag and the adopted distance to NGC 5480 were given as input parameters. The *U*- and *B*-band magnitudes were extrapolated by assuming a constant color during the late phases. The flux integration was performed only over the optical wavelengths. The resultant

Table 4
Estimated Explosion Epoch of SN 2017iro Using Different Methods (see Section 3.1)

Method Adopted	Explosion Epoch
Power-law [$L(t) = A \times (t - t_0)^{0.78}$] fit	JD 2,458,077.1 (2017 November 19.6)
Analytical fit (Taddia et al. 2018)	JD 2,458,080.0 (2017 November 22.5)
Toy model fit (Valenti et al. 2008)	JD 2,458,084.0 (2017 November 26.5)
Mean explosion epoch	JD 2,458,080.4 (2017 November 22.9)

quasi-bolometric LCs of SN 2017iro and well-studied Type Ib events (estimated similarly) are shown in Figure 4. Furthermore, the blackbody fit parameter (temperature and radius), which is a default outcome of the code, is also plotted in Figure 5.

We fitted the Taddia et al. (2018) equation to the quasi-bolometric LC of SN 2017iro and estimated parameters listed in Table 5. The LC peaked at JD 2,458,095.7 with $\log_{10} L = 42.39 \pm 0.09$ erg s^{-1}. The $\Delta m_{15_{\rm bol}}$ value of SN 2017iro is 1.05 mag, which is higher than that of SN 2009jf (0.60 mag) but is comparable to that of SN 2007Y (0.80 mag). The decay rates after +40 days of SN 2017iro (0.016 mag day^{-1}) and SN 2009jf (0.014 mag day^{-1}) are similar, implying relatively faster evolution than the cobalt decay rate (∼0.01 mag day^{-1}; see also Section 5.1). This decay rate is consistent with the range 0.014–0.018 mag day^{-1} seen in Type Ib events (Taddia et al. 2018).

4. Spectroscopic Evolution

The early (photospheric phase) spectra are useful to examine the outermost regions of the expanding ejecta. For example, the presence/absence of residual hydrogen and/or helium during the pre-explosion stellar evolution can be explored with the early-phase spectra. In the nebular phase, because of expansion, the ejecta becomes optically thin, and hence spectra during this phase provide essential information about the inner layers of the ejecta.

In this section, the spectral evolution of SN 2017iro covering the pre-maximum to the nebular phase is presented. The densely sampled spectroscopic data provided an opportunity to compare important spectral features with other well-studied events. All spectra were corrected for the heliocentric velocity of 1856 km s^{-1} of the host galaxy (NGC 5480). The evolution of spectroscopic features is discussed in the following sections.

4.1. Pre-maximum and Early Post-maximum Phase

The spectral evolution in the pre-maximum phase and around the maximum phase is shown in Figure 6 (top panel). During early phase (i.e., pre-maximum), spectroscopy of SN 2017iro was done almost every night. The first spectrum at ∼−7 days clearly shows the broad absorption feature of the He I λ5876 line and weak signatures of other He I lines. He I λ6678 is blended with the narrow Hα line from the host galaxy, whereas the He I λ7065 feature lies at the edge of the telluric absorption band at 6870 Å. Other narrow lines (Hβ λ4861, [N II] λ6584, and [S II] λλ6717, 6731) originating from the underlying H II region are also clearly visible. In the extreme blue region of the observed spectra, well-developed Ca II H and K lines (λλ3934 and 3968) are seen. The spectrum also shows features of the Fe II triplet (λλ4924, 5018, and 5169), Si II λ6355, and a weak absorption due to the Ca II near-IR (NIR) triplet (λλ8498, 8542, and 8662).

In the pre-maximum spectral evolution, the region between 4000 and 4300 Å appears flat, possibly due to the blending of metal lines in the spectra. The absorption around 4400 Å is possibly a blend of He I, Fe II, and Mg II. As the SN evolves toward the maximum, the lines due to He I, Fe II, and Si II become more prominent. In the early post-maximum spectra, the Si II λ6355 feature starts weakening and vanishes in the spectra obtained on +18 days (see Figure 6, bottom panel). A feature around 5500 Å begins to develop in the spectrum of ∼+6 days, which is likely a blend of Fe II λ5535 and Sc II λ5527 lines. The Na I D lines from the host galaxy are seen as a narrow absorption in the spectra.

The spectra of SN 2017iro during the pre-maximum (Figure 7, panel (a)) and close to maximum phase (Figure 7, panel (b)) are compared with the spectra of other well-studied Type Ib SNe, SN 2009jf (Sahu et al. 2011), iPTF13bvn (Srivastav et al. 2014; Kuncarayakti et al. 2015), SN 2007Y (Stritzinger et al. 2009), SN 2008D (Modjaz et al. 2009), and SN 2012au (Pandey et al. 2021), around similar epochs. Good similarity can be noticed in the spectrum of SN 2017iro obtained at −7 days and near maximum with those of SN 2009jf and iPTF13bvn. Except for iPTF13bvn, the Fe II line near 5000 Å is found to be prominent in other SNe used in comparison (see panel (a) in Figure 7). However, in SN 2017iro, the Fe II line appears to be contaminated by the narrow Hβ line from the underlying H II region. The spectrum of SN 2012au is shifted blueward (see panel (b) in Figure 7) owing to its higher expansion velocity (Takaki et al. 2013; Milisavljevic et al. 2013b).

4.2. Late Post-maximum and Early Nebular Phase

The spectral evolution during +18 to +53 days is displayed in the bottom panel of Figure 6. The continuum becomes redder during this phase, the Ca II H and K lines disappear, and other metallic lines appear in this part of the spectrum. However, the region below 4500 Å in our spectrum is noisy, so lines could not be identified. The He I lines are initially prominent, but beyond +45 days, they weaken. In the blue wing of the He I λ5876 line, lines due to Sc II start emerging. The Fe II lines around 5000 Å also start blending. The Ca II NIR triplet gradually transformed into being emission dominated. Beyond +40 days, when the LC enters into the exponential decline, the forbidden lines [O I] λλ6300, 6364 and [Ca II] λλ7291, 7324 start appearing.

From the LC, it is clear that the SN entered into the linear decline phase beyond 50 days after the explosion, which indicates a transition from the photospheric phase to the nebular phase. The emergence of nebular lines, especially the forbidden lines of [O I] λλ6300, 6364 and [Ca II] λλ7291, 7324, also signifies the transition to the nebular phase. The

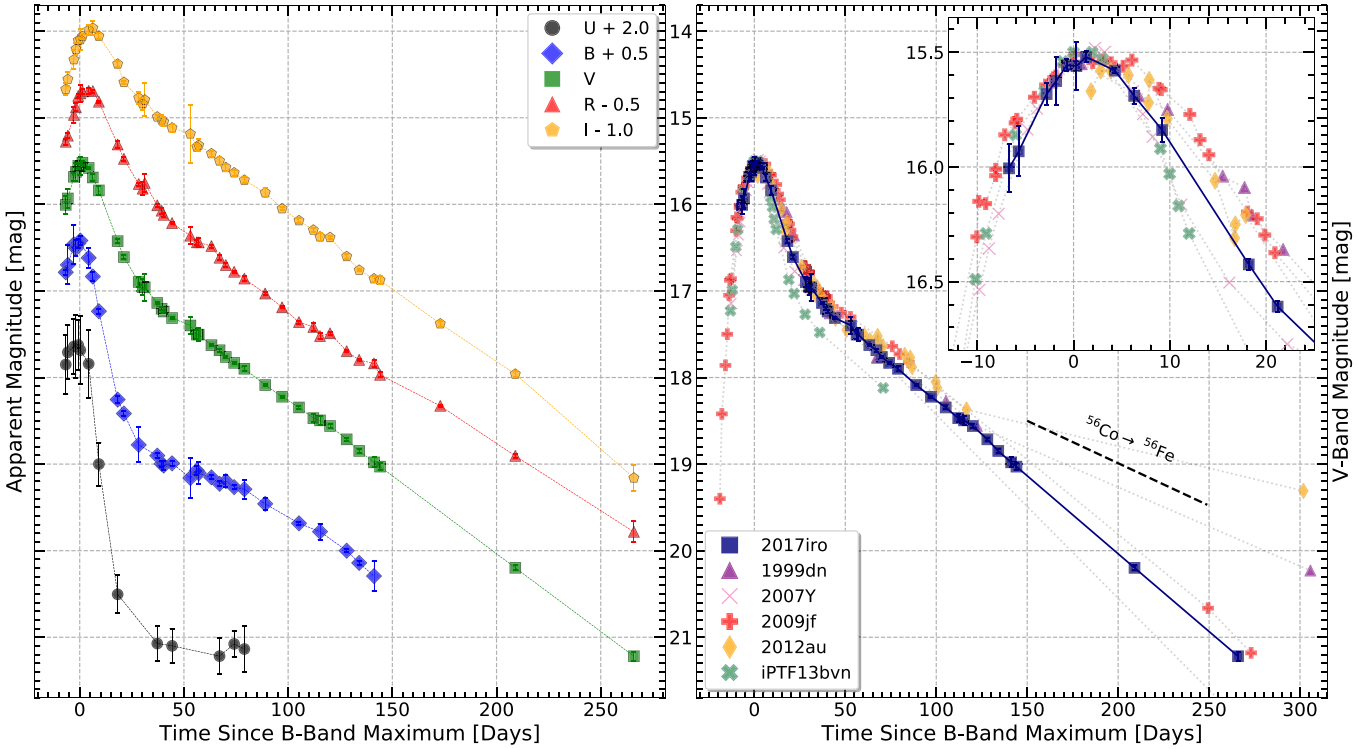

Figure 2. Left panel: the observed *UBVRI* LCs of SN 2017iro. For clarity, the LCs in different bands have been shifted vertically by the indicated amount. Right panel: the *V*-band magnitude of SN 2017iro is overplotted with other Type Ib events, i.e., iPTF13bvn, SN 2012au, SN 2009jf, SN 2007Y, and SN 1999dn (see Table 6 for references). The LCs of other events have been shifted arbitrarily to match the date of maximum and the peak magnitude to SN 2017iro. The evolution of LCs near the peak is also shown in the inset.

spectrum taken during +67 to +112 days is displayed in Figure 8. During this phase, the spectra are slowly getting dominated by the forbidden emission lines. The nebular line [O I] λ5577 is also seen along with the O I λ7774 line, which is probably powered by an oxygen recombination cascade. The Ca II NIR triplet is dominated by the emission component and possibly blended with the [C I] λ8730 line. The spectrum obtained on +112 days still shows the presence of continuum and is not fully nebular. In Figure 7 (panel (c)), the spectra near a month after the maximum light are compared. The ∼+31 day spectrum of SN 2017iro is similar to the spectra of iPTF13bvn and SN 2008D. Also, He I $\lambda\lambda$6678, 7065 lines in SN 2009jf are weaker as compared to other SNe. It is also worth mentioning that between 4000 and 5000 Å SN 2017iro and SN 2008D exhibit comparatively flat structures, but iPTF13bvn and SN2009jf have strong features in this wavelength range.

4.3. Nebular Phase

The spectra taken during +134 to +209 days are presented in Figure 9. The spectra are dominated by the forbidden emission lines of [O I] and [Ca II]; narrow lines from the nearby H II region are also clearly seen. The [O I] λ5577 line, which was fairly strong in the early nebular phase (before ∼100 days), faded after that and almost vanished in the nebular spectra. The semi-forbidden line Mg I] λ4571 is found to be always weak in the spectra of SN 2017iro. The emission component of the Ca II NIR triplet, which was stronger until ∼120 days, starts weakening, and by ∼176 days it merges with the almost flat continuum. The forbidden [O I] and [Ca II] lines show a complex profile.

In Figure 10, the nebular phase spectrum of SN 2017iro at +209 days is compared with those of other Type Ib events, obtained at similar epochs. The emission features of semi-forbidden Mg I] λ4571, forbidden [O I] $\lambda\lambda$6300, 6364, and [Ca II] $\lambda\lambda$7291, 7324 lines are prominently visible in these SNe. It is interesting to note that in SN 2017iro the strengths of [O I] and [Ca II] lines are similar, whereas in SN 2009jf, SN 2012au, and Master OT J120451.50+265946.6 (MOT) the [O I] line is stronger than the [Ca II] line. In SN 2017iro, the Mg I] is comparatively much weaker than in other SNe. The ratio of Mg I] to [O I] lines in SN 2017iro is estimated as ∼0.15, which is similar to that of MOT (∼0.3; Singh et al. 2019) but less than that of iPTF13bvn (∼0.85; Kuncarayakti et al. 2015).

Among the nebular forbidden emission lines, the Mg I] line lies in the bluer and crowded region of the spectra, where generally signal is poor. Furthermore, Ca is a trace element, and its distribution is not necessarily representative of the bulk of the ejecta. Hence, the [O I] doublet, which emerges in a relatively clear region, is generally used as the tracer of the explosion geometry (Mazzali et al. 2005; Maeda et al. 2008; Modjaz et al. 2008; Taubenberger et al. 2009; Milisavljevic et al. 2010). From Figure 10, similarity between nebular spectra of SN 2009jf and SN 2017iro is evident, with the [O I] line profile being asymmetric and multipeaked in both objects. However, asymmetry in the [O I] line profile of SN 2017iro is weaker as compared to SN 2009jf, with the peaked component of the [O I] line centered at rest wavelength. The asymmetric and multicomponent [O I] profile, seen in the nebular spectra, can be reproduced with a complex ejecta geometry of an aspherical explosion (Mazzali et al. 2005; Maeda et al. 2007b). The observed features in the asymmetric [O I] line profile in SN 2017iro could be explained with a high-density core of the ejecta (Taubenberger et al. 2009; Maeda et al. 2008).

Table 5
Light-curve Parameters of SN 2007iro (see Section 3.2)

Filter	Max Epoch (JD)	m_{max} (mag)	Δm_{15} (mag)	Δm_{40} (mag)	Late-time Slope (∼40–140 days) (mag 100 day^{-1})	Late-time Slope (>140 days) (mag 100 day^{-1})	$\Delta d_{0.25}$ (days)
U	2,458,095.7 ± 0.5	15.57 ± 0.01	2.41 ± 0.07	3.55 ± 0.01	⋯	⋯	7.70 ± 0.14
B	2,458,096.2 ± 0.5	15.94 ± 0.01	1.46 ± 0.05	2.44 ± 0.01	1.27	⋯	10.40 ± 0.14
V	2,458,098.0 ± 0.5	15.55 ± 0.01	0.77 ± 0.04	1.70 ± 0.01	1.73	1.80	11.90 ± 0.14
R	2,458,099.4 ± 0.5	15.14 ± 0.01	0.69 ± 0.02	1.54 ± 0.01	1.57	1.52	12.20 ± 0.14
I	2,458,100.5 ± 0.5	14.97 ± 0.01	0.52 ± 0.02	1.14 ± 0.01	1.75	1.90	14.70 ± 0.14
Bolometric	2,458,095.7 ± 0.5	16.12 ± 0.01	1.05 ± 0.04	1.89 ± 0.01	1.65	⋯	10.40 ± 0.14

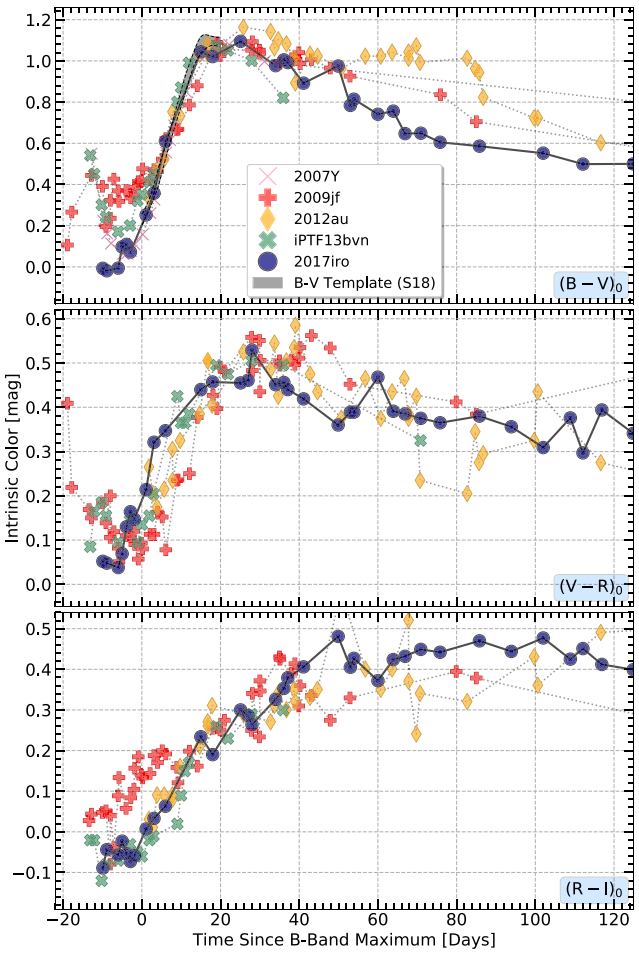

Figure 3. Color evolution of SN 2017iro, plotted along with iPTF13bvn, SN 2012au, SN 2009jf, SN 2007uy, and SN 2007Y. Both the Milky Way and the host galaxy extinction corrections have been applied for each SN. The $B-V$ color templates from Stritzinger et al. (2018) are overplotted in the top panel for comparison. The bibliographic sources are the same as mentioned in the text (Section 3).

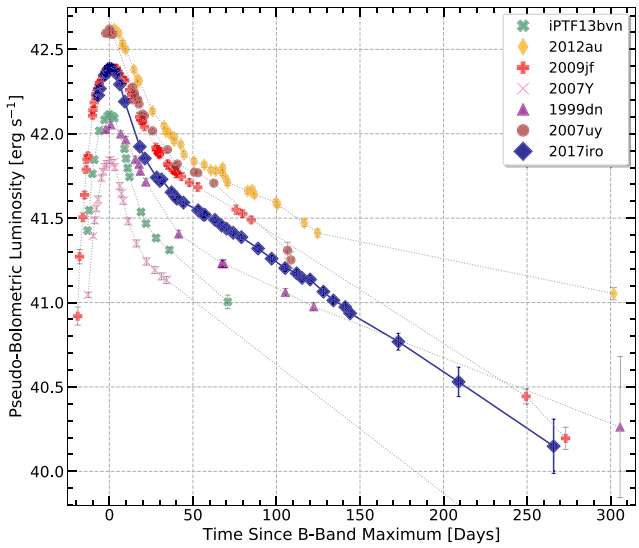

Figure 4. The pseudo-bolometric LC of SN 2017iro (connected with a bold line) compared with those of other, similar Type Ib events (iPTF13bvn, SN 2012au, SN 2009jf, SN 2007uy, SN 2007Y, and SN 1999dn). The pseudo-bolometric LCs were obtained using SUPERBOL.

Table 6
Sample of Type Ib SNe Used in This Study

Name	$E(B-V)_{tot}$ (mag)	Distance (Mpc)	References
SN 1999dn	0.10	38.90	1
SN 2007Y	0.11	19.31	2
SN 2007uy	0.63	29.50	3
SN 2009jf	0.11	34.25	4, 5
SN 2012au	0.06	23.50	6, 7
iPTF13bvn	0.22	22.49	8, 9

References. (1) Benetti et al. (2011); (2) Stritzinger et al. (2009); (3) Roy et al. (2013); (4) Sahu et al. (2011); (5) Valenti et al. (2011); (6) Milisavljevic et al. (2013b); (7) Takaki et al. (2013); (8) Srivastav et al. (2014); (9) Kuncarayakti et al. (2015).

The gas-phase oxygen abundance in the vicinity of the SN location is estimated using the relation of Pettini & Pagel (2004). N2 and the O3N2 indices were computed from the last spectrum obtained on ∼209 days. The average value of oxygen abundance 12 + log(O/H) (estimated using O3N2 and N2 indices) for the SN region is found to be 8.64 ± 0.2, which is remarkably similar to iPTF13bvn (8.63; Kuncarayakti et al. 2015). In a recent study under the CALIFA (Sánchez et al. 2012) survey program, Galbany et al. (2016) used wide-field integral field spectroscopy to compute the global metallicity of NGC 5480 and metallicity at the location of SN 1988L. The estimated values are 8.58 and 8.55 for the local and global, respectively. This shows that our estimate of the oxygen abundance is in fairly good agreement with the previous study and is close to the solar value of 12 + log (O/H) = 8.69 ± 0.05 (Asplund et al. 2009). Further, the computed metallicity close to the SN location is similar to the estimates of Modjaz et al. (2011; 8.49 ± 0.19) and Sanders et al. (2012; 8.48 ± 0.16), made at the location of other SNe Ib.

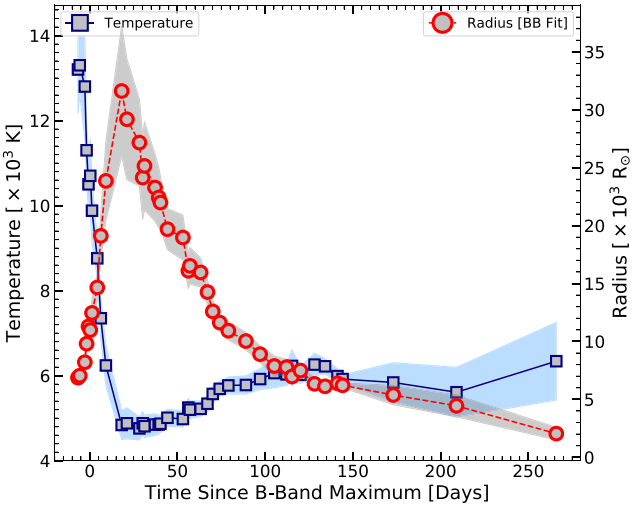

Figure 5. The blackbody temperature and radius evolution of SN 2017iro. These parameters were derived from the photometric data using SUPERBOL. The shaded regions indicate 1σ uncertainties.

4.4. Line Velocities

The velocities of lines Fe II λ5169, He I λ5876, He I λ6678, and Si II λ6355 were estimated by fitting a Gaussian profile to the respective absorption trough after correcting the spectra for the redshift of the host galaxy of SN 2017iro. The estimated line velocities of SN 2017iro, along with those of SN 2007Y, SN 2008D, SN 2009jf, SN 2012au, and iPTF13bvn, collected from the literature are plotted in Figure 11. In the case of SN 2017iro, the He I λ5876 velocity is $\sim$11,500 km s^{-1} in the beginning and declined to $\sim$9000 km s^{-1} near maximum. In the post-maximum phase, it evolves slowly and becomes flat ($\sim$7000 km s^{-1}) after +70 days. All the SNe (except SN 2007Y) used in the comparison show a steep decline in the He I λ5876 line velocity during the pre-maximum phase. The post-maximum evolution of He I shows a modest increase of $\sim$900 km s^{-1}, giving rise to a bump-like feature in the velocity evolution. A similar feature can also be seen in SN 2009jf, iPTF13bvn, and SN 2008D during maximum to $\sim$+20 days. The origin of this feature needs to be explored. The evolution of the He I λ5876 line velocity beyond $\sim$+25 days is similar to that in SN 2017iro, iPTF13bvn, and SN 2009jf but lower than that of SN 2012au. In homologous expanding SNe ejecta, it is difficult to accurately determine the photospheric velocity from the observed spectral features, as no measurable feature of the spectra is connected directly to photospheric velocity (Takáts & Vinkó 2012). However, the prominent absorption features produced owing to Fe II λ5169 can be used as a good tracer of SN photospheric velocity, as it is a less optically thick line compared to several other lines (Dessart & Hillier 2005). The Fe II line velocity of SN 2017iro is compared in the middle panel of Figure 11. The ejecta velocity measured using the Fe II line of all the SNe shows a steep decline until $\sim$+25 days and flattens thereafter. The Fe II line velocity of SN 2017iro near maximum is comparable to those of SN 2007Y, SN 2009jf, and iPTF13bvn but slower than those of SN 2008D and SN 2012au. In the later phase (>+25 days), the Fe II line velocity of SN 2017iro is in between those of SN 2009jf and SN 2007Y. The Fe II velocity around maximum light ($\sim$9000 $\pm$ 800 km s^{-1}) is used to estimate the explosion energy of SN 2017iro (see Section 5.3).

5. Discussion

The observed fraction of Type Ib SNe is low, as they are rare objects (Li et al. 2011; Graur et al. 2017a, 2017b; Shivvers et al. 2019). There are only a handful of events for which studies covering both photospheric and nebular phases are available. A detailed investigation of SN 2017iro, hence, is a good addition to this sample, as it fills the gap between fast-declining (e.g., SN 2007Y, iPTF13bvn) and slow-declining (e.g., SN 2009jf) objects (see Section 3.2). Here we discuss the nature of SN 2017iro based on some significant LC and spectral features, constrain its progenitor mass, and also estimate the explosion parameters.

5.1. Late-phase Light-curve Heterogeneity

The LC of SE-SNe follows a linear decline with the onset of the nebular phase (usually >100 days after the explosion). This is a consequence of energy injection from the radioactive decay of ^{56}Co $\rightarrow$ ^{56}Fe. The efficiency of γ-ray trapping within the ejecta affects the decay rate. In general, it is found that the late-phase LC of SE-SNe declines faster than the expected decay rate of 0.98 mag (100 days)$^{-1}$ from ^{56}Co $\rightarrow$ ^{56}Fe transition. This is primarily due to the lower opacity of the ejecta for the γ-rays (i.e., incomplete trapping). Therefore, the LC decay rate during the nebular phase can be used to infer the ratio of explosion energy and mass of the ejecta. The late-phase (beyond 140 days) decline rate of SN 2017iro is estimated in different bands and is listed in Table 5. The LCs are found to decline significantly faster than 0.98 mag (100 days)$^{-1}$.

An investigation of the late-time LC of SE-SNe by Wheeler et al. (2015) revealed the diverse nature of their evolution, indicating dispersion in the ejecta masses and kinetic energies. Our comparison of the late-time decay rate of well-studied Type Ib SNe (see Figure 2, right panel) indicates that there exist two groups of events. SN 1999dn and SN 2012au fall under the first category, in which the late-phase decline rate is significantly slower than the ^{56}Co $\rightarrow$ ^{56}Fe decay rate. The slower LC decline rate indicates the need for an additional source of energy, which could be interaction of the ejecta with the circumstellar material (CSM), a magnetar, or the presence of a light echo. Wheeler et al. (2015) suggested the presence of CSM in SN 1999dn. The presence of smoothly distributed CSM around SN 2012au was inferred from its detection in radio wave bands (Kamble et al. 2014). However, very late nebular spectra of SN 2012au, obtained $\sim$6.2 yr after the explosion, indicated magnetar/pulsar wind nebulae as the most probable energy source (Milisavljevic et al. 2018). In the second group of SE-SNe, the LC decline rate is faster than the expected decline rate of ^{56}Co–^{56}Fe. The faster decline rate could be due to incomplete trapping of γ-rays produced via ^{56}Co–^{56}Fe decay, in the SN ejecta. The late-time decay rate of SN 2017iro indicates that it falls in this category and is similar to those of SN 2009jf, SN 2007Y, and iPTF13bvn. It is worth mentioning that during the late nebular phase an increasing fraction of photons emitted at IR wavelength may also steepen the decline rate in optical bands.

5.2. ^{56}Ni Mixing

The lines of He I, the identifying features of Type Ib SNe, are seen at a velocity of $\sim$11,500 km s^{-1} in the first spectrum ($\sim$−7 days) of SN 2017iro (see Figure 11). The origin of these lines requires nonthermal excitation and ionization (Lucy 1991;

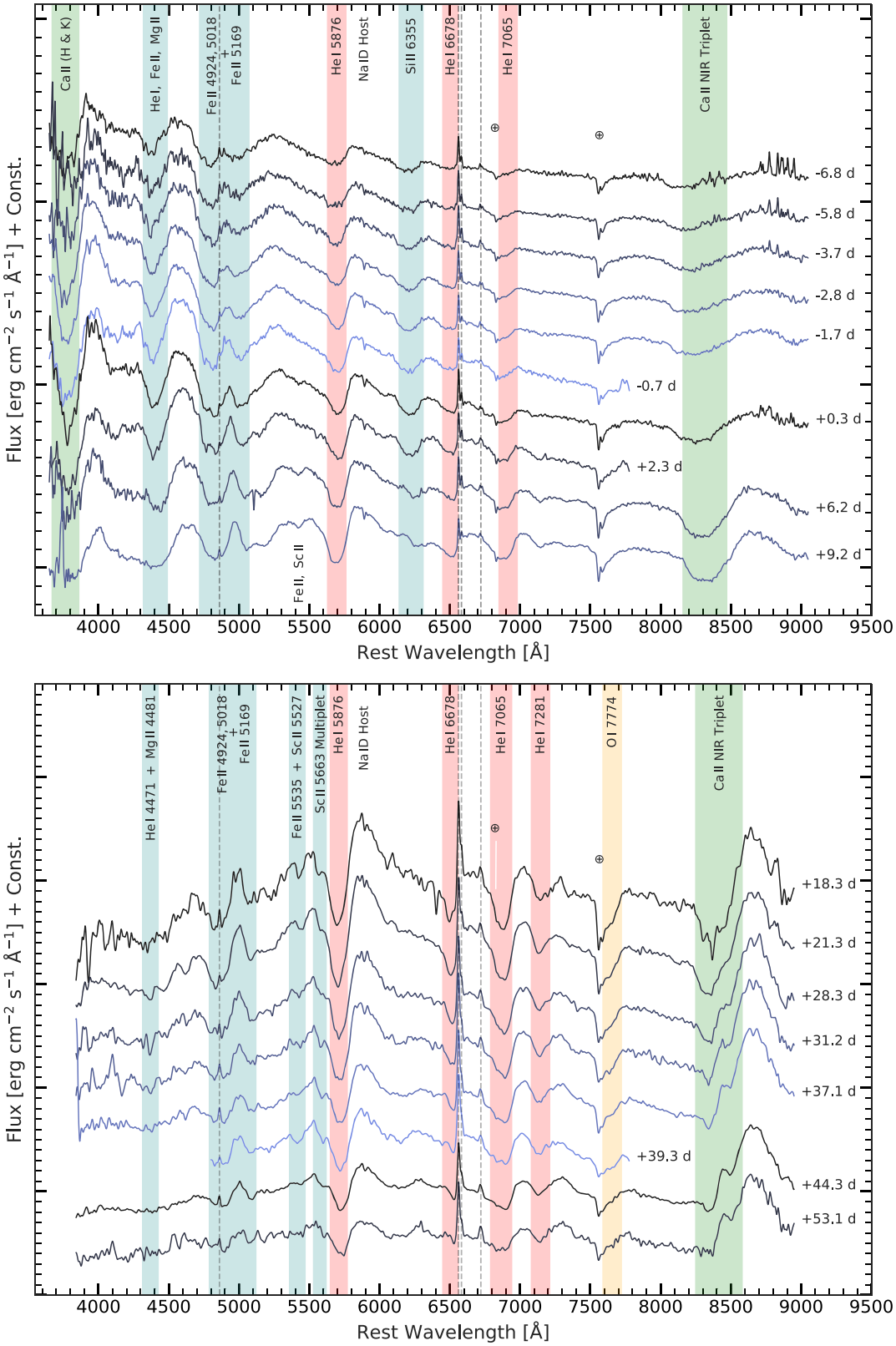

Figure 6. The early (−7 to +9 days) and late (+18 to +53 days) phase spectral evolution of SN 2017iro are displayed in the top and bottom panels, respectively. Prominent spectral lines are marked. The labeled phases are with respect to the *B*-band maximum (JD 2,458,096.2). The spectra have been corrected for redshift and reddening. Features arising from the host are marked with dashed vertical lines. Major telluric bands are shown with a circled plus sign. The spectra shown in Figures 6, 8, and 9 are available as data behind the figure.

(The data used to create this figure are available.)

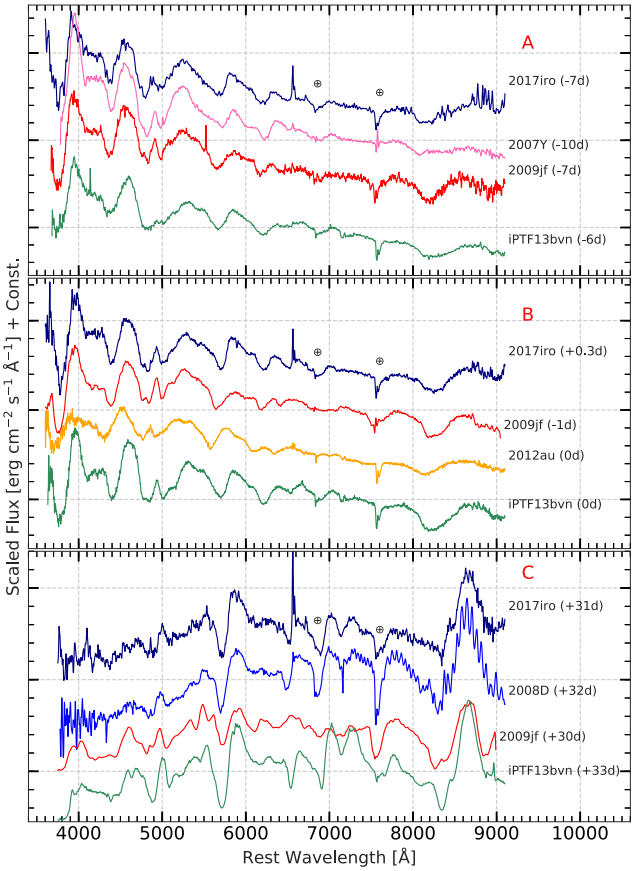

Figure 7. SN 2017iro spectral evolution compared with other Type Ib events (iPTF13bvn, SN 2012au, SN 2009jf, SN 2008D, and SN 2007uy) at similar epochs. Panels (a), (b), and (c) represent the pre-maximum, near-maximum, and post-maximum spectra, respectively. Telluric lines are shown with circled plus signs.

Swartz 1991). The accelerated electrons responsible for the nonthermal excitation are regulated by the γ-rays produced in the radioactive decay of newly synthesized ^{56}Ni (Harkness et al. 1987). It is shown that the mere presence of an appreciable amount of helium in the progenitor would not lead to the presence of helium lines in the spectra (Dessart et al. 2012). To excite He I at high velocities, γ-rays need to be in the proximity of the helium layer, either due to the leakage of γ-rays through the inner ejecta or by substantial mixing of ^{56}Ni up to the outer ejecta.

Mixing may arise for various reasons, such as large-scale asymmetric explosion jets, asymmetry of the propagating shock, etc. (see Maund et al. 2009; Couch et al. 2011; Dessart et al. 2012, and references therein). The effect of ^{56}Ni mixing on the LCs and spectra of SE-SNe have been investigated in detail by several authors. Theoretical studies (Shigeyama et al. 1990; Hachisu et al. 1991) argued that ^{56}Ni mixing within the helium layer might depend on the progenitor composition. The degree of ^{56}Ni mixing may also significantly influence the overall LC shape (including the post-maximum phase) and the efficient formation of He I spectral lines (Ensman & Woosley 1988; Woosley & Eastman 1997; Shigeyama et al. 1990; Cano et al. 2014; Dessart et al. 2015, 2016; Taddia et al. 2018).

The early-time color evolution of Type Ib/c SNe can also be used as a diagnostic for the ^{56}Ni distribution in the ejecta. It is shown that in the case of strong mixing the color curves of Type Ib/c SNe monotonically redden during the photospheric phase, because of continuous and progressive effects of ^{56}Ni heating, whereas in the case of weak to moderate mixing the color evolution does not show monotonic behavior owing to delayed heating from ^{56}Ni (Yoon et al. 2019, and references therein). The early-phase $B-V$ colors of different Type Ib events, along with ^{56}Ni mixing models (Yoon et al. 2019), are plotted in Figure 12. The color evolution of SN 2007Y, SN 2009jf, and iPTF13bvn follows a nonmonotonic trend, which is interpreted in the framework of weak to moderate mixing of ^{56}Ni in the ejecta. However, the nonavailability of sufficiently early phase data points for SN 2017iro prevents us from arriving at any firm conclusion on the role of mixing.

5.3. Physical Parameters of Explosion

The peak of the LC and its shape in SE-SNe are mainly regulated by the synthesized radioactive ^{56}Ni, kinetic energy (E_k), and ejecta mass ($M_{\rm ej}$). Estimation of these parameters is crucial in understanding the explosion properties. The explosion parameters can be derived either employing detailed hydrodynamical modeling of both the LC and the spectra or using semianalytical models. In the present study, several semianalytical formulations were used to fit the quasi-bolometric LC (see Section 3.4) of SN 2017iro.

5.3.1. Estimation of ^{56}Ni Mass, Ejecta Mass, and Kinetic Energy

The optically thick phase of the LC (photospheric phase) was fitted by the formulation originally proposed by Arnett (1982) and later updated by Valenti et al. (2008). Major assumptions in this analytical approach comprise a small radius of the progenitor, spherical symmetry and homologous expansion of the ejecta, constant opacity ($\kappa_{\rm opt}$), and a centrally located and unmixed ^{56}Ni (see Arnett 1982; Valenti et al. 2008; Cano 2013). The parameters $M_{\rm Ni}$ (nickel mass) and τ_m (diffusion timescale) were kept as free variables while obtaining the fit. Considering a uniform density medium, the ejecta kinetic energy E_k and τ_m are given by

$$\tau_m = \sqrt{2}\left(\frac{\kappa_{\rm opt}}{\beta c}\right)^{1/2}\left(\frac{M_{\rm ej}}{v_{\rm ph}}\right)^{1/2}, \quad (1)$$

$$E_k \approx \frac{3}{5}\frac{M_{\rm ej}v_{\rm ph}^2}{2}, \quad (2)$$

where $\beta \approx 13.8$ is a constant of integration (Arnett 1982) and c is the speed of light. The optical opacity $\kappa_{\rm opt}$ is adopted as 0.07 cm^2 g^{-1} (e.g., Chugai 2000; Toy et al. 2016; Taddia et al. 2018). The quasi-bolometric LC of SN 2017iro until 30 days from the explosion epoch was fitted using least-squares optimization. The best fit was obtained for $M_{\rm Ni} = 0.09 \pm 0.04\,M_\odot$ and $\tau_{\rm m} = 9.95 \pm 0.44$ days. The derived ^{56}Ni mass was further estimated using the bolometric rise time of 16.5 days and a peak bolometric luminosity $\log_{10} L = 42.39$ erg s^{-1}. The relation given by Stritzinger & Leibundgut (2005) gives a value of 0.10 ± 0.01 $M_\odot$. Using the measured Fe II line velocity 9000 km s^{-1} near the bolometric maximum (see Section 4.1), the $M_{\rm ej}$ and E_k are estimated as 1.39 $M_\odot$ and 0.75×10^{51} erg, respectively.

While investigating the physical parameters of SN 2002ap, Vinkó et al. (2004) proposed analytic models for post-maximum phase with assumptions as described in the beginning of this subsection. In brief, these models are based

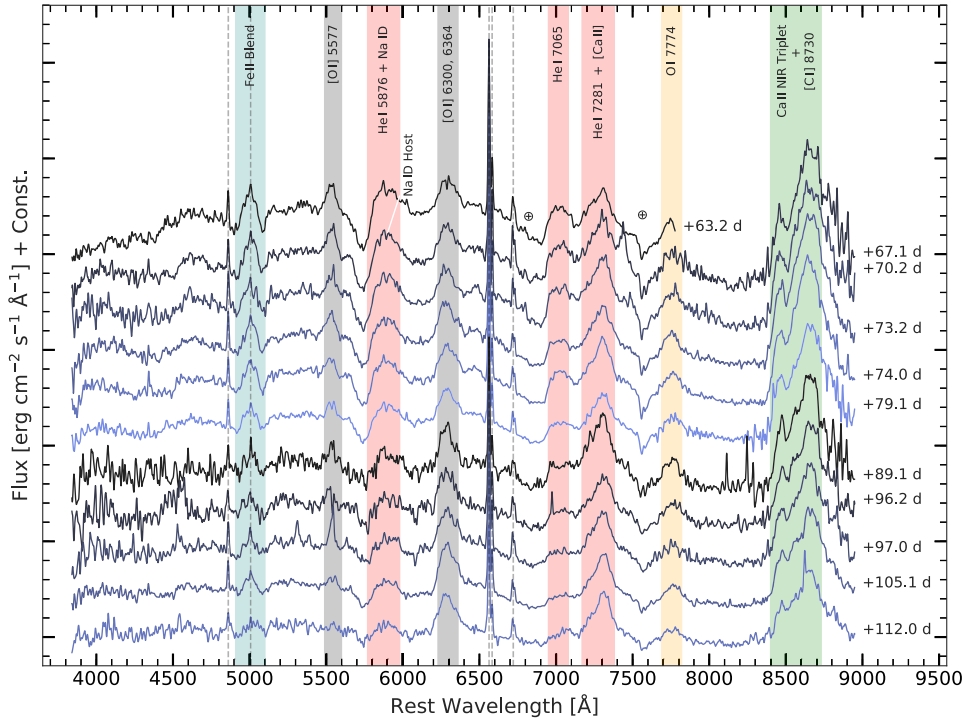

Figure 8. Late post-maximum and early nebular phase (∼+67 to +112 days) spectral evolution of SN 2017iro. Prominent spectral lines are also marked. Other descriptions are similar to those mentioned in Figure 6. The spectra shown in Figures 6, 8, and 9 are available as data behind the figure.

on the ejecta density configuration characterized by x_0 (fractional radius of the core) and n (power-law exponent) parameters. We used their model C1, which represents a "core–shell" structure with a fixed density core of fractional radius, $x_0 = 0.15$, and a fixed value of $\kappa_\gamma = 0.027\,\mathrm{cm^2\ g^{-1}}$ for gray atmospheres (Sutherland & Wheeler 1984). The best-fit model is shown in Figure 13 with $M_{\rm ej} = 4.3\,M_\odot$, $M_{\rm Ni} = 0.05\,M_\odot$, $E_k = 1.85$ foe, and $v_{\rm max} = 8500\ \mathrm{kms^{-1}}$.

Energy production rates of the $^{56}\mathrm{Ni} \rightarrow {}^{56}\mathrm{Co} \rightarrow {}^{56}\mathrm{Fe}$ decay chain computed by Nadyozhin (1994) were further used to examine the mass of synthesized ^{56}Ni during the explosion. The energy production curves for three different values (i.e., 0.06, 0.10, and 0.15 $M_\odot$) of the mass of ^{56}Ni were overplotted in Figure 13. The maximum in the quasi-bolometric LC describes roughly the transition between the emission deficit due to the large optical depth (larger diffusion timescale) and an excess emission due to the stored radiation post-maximum. The early post-maximum decline can be approximated by the instantaneous energy production rate of $^{56}\mathrm{Ni} \rightarrow {}^{56}\mathrm{Co}$ decay. Hence, we infer that 0.10 $M_\odot$ of ^{56}Ni was synthesized in the explosion owing to its best match to the initial post-maximum decline of the quasi-bolometric LC of SN 2017iro. The large discrepancy between the energy production rate and the quasi-bolometric luminosity during the late phase is arising owing to the escape of gamma rays.

Based on a study of 38 SE-SNe, Lyman et al. (2016) proposed a fitting relation to estimate $M_{\rm Ni}$ (see their Equation (4)). To populate this data sample, we collected nine additional SE-SNe (five IIb, two BL-Ic, one Ic-transitional, and one Ib) with well-sampled LCs from the literature (see Table 7). Also, to estimate $M_{\rm bol}$, the data available only in the optical wavelength were used. In Figure 14, a correlation between $M_{\rm bol}$ and ^{56}Ni mass is shown for all 47 events. The plot also indicates that among the population of SE-SNe the Type IIb events produce a lesser amount of ^{56}Ni. However, there appears to be no significant difference in ^{56}Ni production between Type Ib and Ic SNe, whereas Type Ic-BL SNe, in general, are brighter with higher ^{56}Ni mass. This is in line with other recent studies (Anderson 2019; Prentice et al. 2019). With an $M_{\rm bol_{peak}}$ of -17.19 ± 0.22 mag (see Table 5) and ^{56}Ni mass of 0.08 $M_\odot$ (average value estimated from above methods), SN 2017iro (shown with a star symbol in the Figure 14) lies near the expected correlation for SE-SNe. It is to be noted here that the explosion parameters inferred using empirical relations are approximate, and detailed hydrodynamical modeling (e.g., Taddia et al. 2018) would be required for better estimates.

5.3.2. Oxygen Mass

The [O I] line flux in the nebular spectra of SE-SNe can be used to estimate the neutral oxygen mass that is required to produce the emission. In the high electron density ($n_e \geqslant 10^{-6}$ cm^{-3}) region, the minimum O mass can be estimated by the relation $M_O = 10^8 \times D^2 \times F([\mathrm{O\ I}]) \times \exp(2.28/T_4)$, provided by Uomoto (1986). Here the mass of neutral oxygen is represented as $M_{\rm O}$ (in $M_\odot$), D is the SN distance (in Mpc), F ([O I]) is the observed absolute flux of the [O I] line (in erg s^{-1} cm^{-2}), and T_4 is the temperature associated with the oxygen-emitting region in units of 10^4 K. The [O I] λ5577 /($\lambda\lambda$6300, 6364) line ratio can be used as a proxy for estimating the temperature. In our nebular phase spectra (see Figure 9), the [O I] λ5577 line is not detected, allowing us to set ∼0.1 as the upper limit for the line ratio. At this limit, the emitting region should either be at a relatively low temperature ($T_4 \leqslant 0.4$) for the high-density limit or be at a low electron density ($n_e \leqslant 5 \times 10^6$ cm^{-3}) if $T_4 = 1$ (Maeda et al. 2007b).

Previous studies have shown that during the nebular phase the temperature of the line-emitting region lies in the range 3400–4200 K (Schlegel & Kirshner 1989; Elmhamdi et al. 2004; Elmhamdi 2011). Assuming that the high-density regime is valid

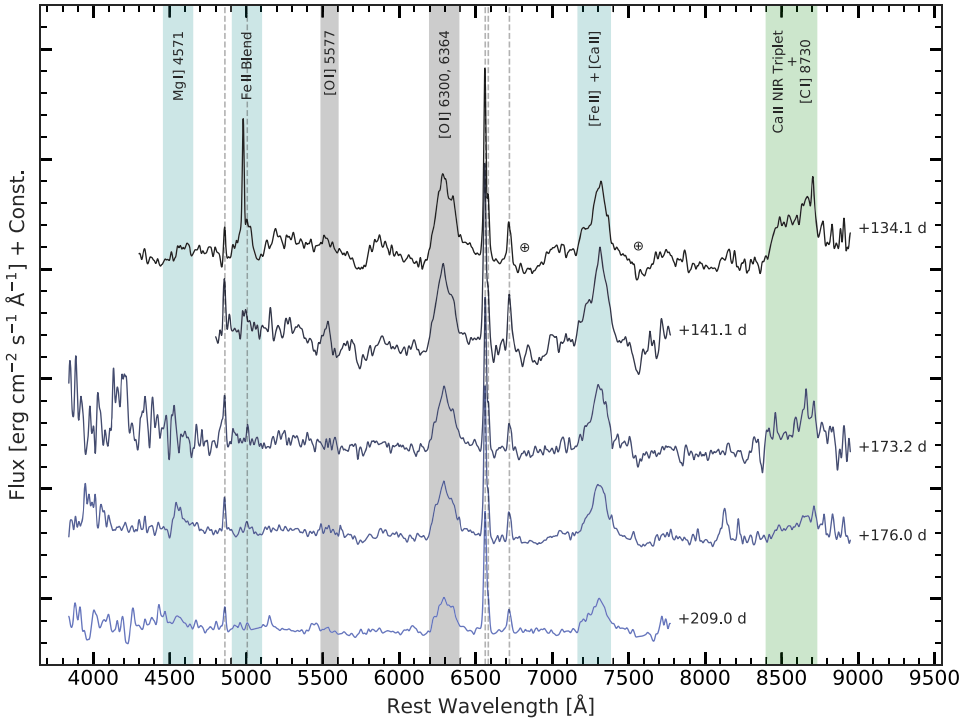

Figure 9. Nebular phase (∼+134 to +209 days) spectra of SN 2017iro. Various nebular emission lines are shown. The dashed vertical lines indicate the features arising from the host, and the telluric bands are shown with a circled plus sign (for other descriptions, see Figure 6). The spectra shown in Figures 6, 8, and 9 are available as data behind the figure.

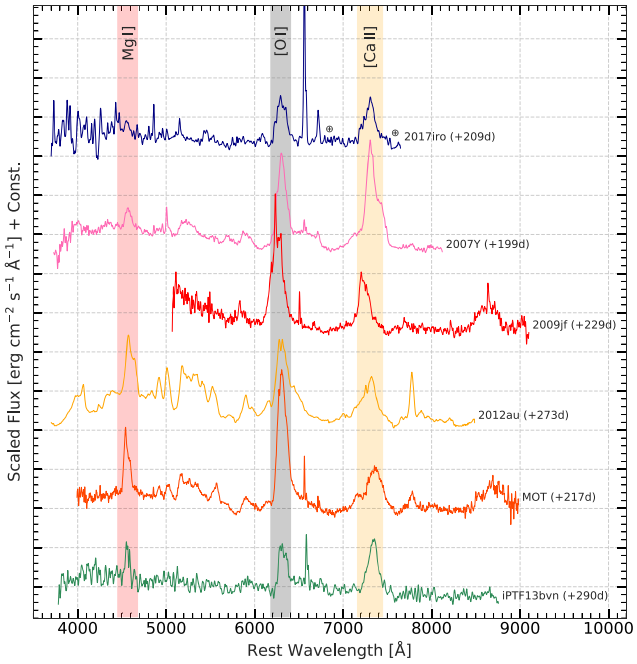

Figure 10. Comparison of nebular phase spectral features of SN 2017iro with other well-studied Type Ib events. The SN references are the same as described in Section 4.1, in addition to Master OT J120451.50+265946.6 (MOT; Singh et al. 2019).

for SN 2017iro, the temperature of the line-emitting region can be taken to be $T_4 = 0.4$. Using the [O I] flux (in the +209 day spectrum) of 1.12×10^{-14} erg s^{-1} cm^{-2}, $D = 30.8$ Mpc, and $T_4 = 0.4$, we calculated the minimum mass of neutral oxygen to be 0.35 $M_\odot$, which is similar to the mass estimated for SN iPTF13bvn (Kuncarayakti et al. 2015). It is to be noted that for different densities the temperature of line-emitting regions may vary (Schlegel & Kirshner 1989; Leibundgut et al. 1991; Sollerman et al. 1998; Elmhamdi et al. 2004; Maeda et al. 2007b). An increase in temperature from 4000 to 4200 K lowers the oxygen mass by a factor of ∼0.8. Similarly, a decrease in temperature from 4000 to 3400 K results in higher oxygen mass by a factor of ∼3. Hence, depending on the assumed temperature and density, the range of oxygen mass spans 0.28–1.05 $M_\odot$. The clumpy nature of the ejecta and the presence of nonoptically thin material (which is not accounted here) may raise this value (Maeda et al. 2007a; Kuncarayakti et al. 2015). In Table 8, the neutral oxygen mass estimates are listed for a few well-studied objects showing a broad range of estimated masses. We admit that the mass of the oxygen estimated here is a lower limit of the total oxygen present in the ejecta of SN 2017iro.

5.4. Nature of the Progenitor Star

Hydrodynamic explosion models suggest that Mg and O should have similar spatial distribution within the SN ejecta of SE-SNe (Maeda et al. 2006). Taubenberger et al. (2009) analyzed a large number of nebular spectra of SE-SNe and inferred that in a majority of cases the line profiles of semi-forbidden Mg I] λ4571 and forbidden oxygen [O I] λλ6300, 6364 lines are similar, confirming the similar distribution of Mg and O in the ejecta. The strength of the Mg I] λ4571 line grows over time in comparison with [Ca II] λλ7291, 7324 and [O I] because the deeper Mg-O layer of the progenitor core becomes visible with time (Foley et al. 2003; Kuncarayakti et al. 2015). SN 2017iro shows a feeble presence of Mg I] λ4571, possibly due to less stripping of its progenitor.

The progenitor mass of a CCSN can be constrained by estimating the [O I] λλ6300, 6364 / [Ca II] λλ7291, 7324 emission-line ratio in the nebular phase (Kuncarayakti et al. 2015). In contrast to Ca, the explosively synthesized O is

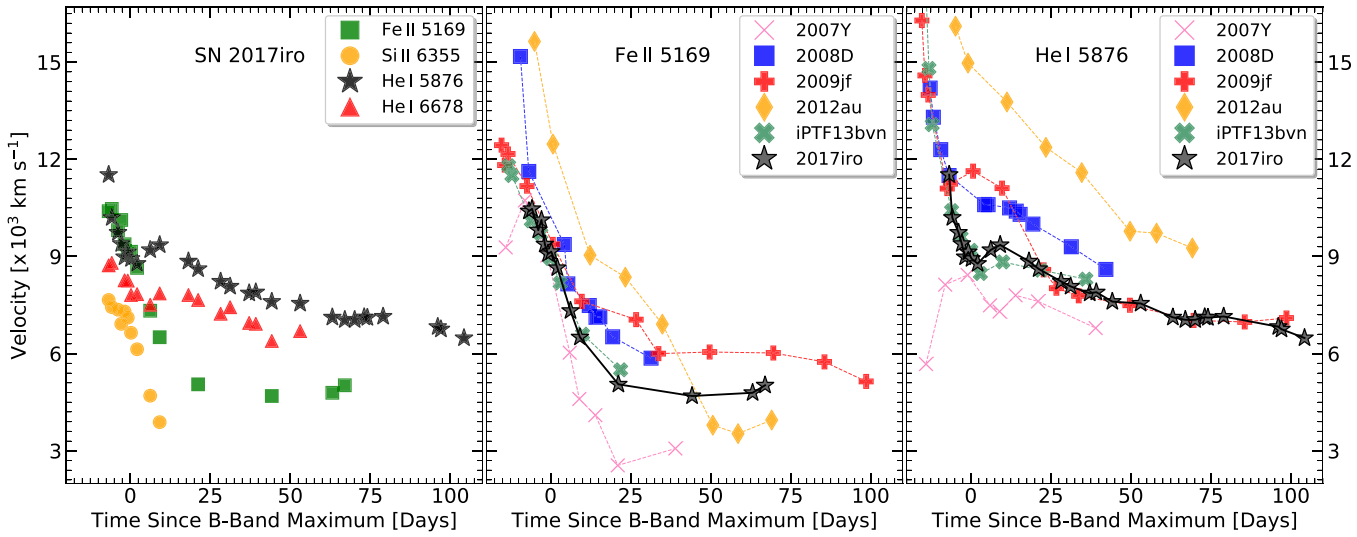

Figure 11. Evolution of the velocity of different spectral lines observed in SN 2017iro. Error in these estimates was never below 800 km s^{-1}. The line velocities of different SNe (SN 2007Y, SN 2008D, SN 2009jf, SN 2012au, and iPTF13bvn) are also compared.

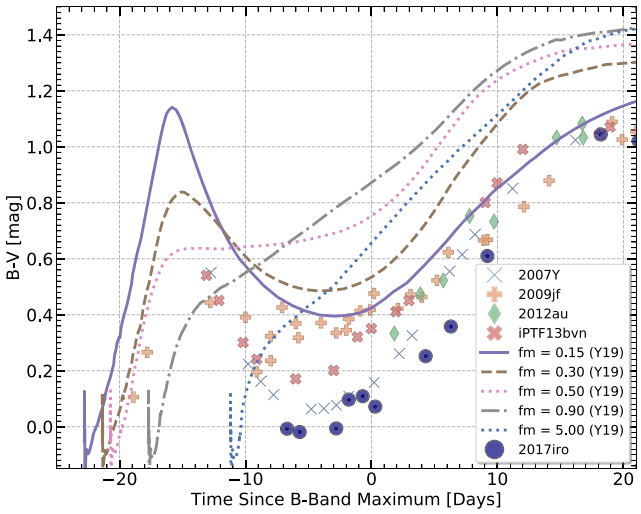

Figure 12. The $B-V$ color evolution of SN 2017iro compared with the synthetic color curves of SN Ib models by Yoon et al. (2019). The five bold curves indicate varying degrees of ^{56}Ni mixing (f_m) as shown in the legend (Y19). An increasing value of f_m implies a stronger ^{56}Ni mixing (for more details, see Yoon et al. 2019).

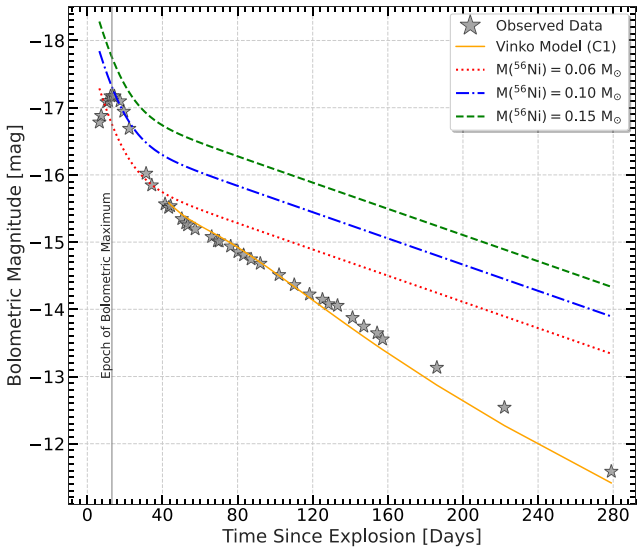

Figure 13. The quasi-bolometric LC of SN 2017iro fitted with analytical model C1 of Vinkó et al. (2004). Three curves (dotted, dashed, and dashed–dotted) representing the rate of energy production for different masses of ^{56}Ni synthesized during the explosion, based on the analytical formulation by Nadyozhin (1994), have also been shown.

sensitive to the main-sequence mass of the progenitor, and therefore a larger value implies a larger core mass (however, mixing can also play a substantial role; see Fransson & Chevalier 1989). Kuncarayakti et al. (2015) compared the [O I] / [Ca II] line ratio of SE-SNe and Type II SNe. They found that the line ratio of Type Ib/c SNe exhibits considerable dispersion. The observed spread in the line ratio cannot be explained by the temporal evolution of the line flux. Instead, it could arise from two different progenitor channels for SE-SNe: a single massive star or a less massive star in a binary system. The [O I] / [Ca II] ratio in the spectra of SN 2017iro obtained between 173 and 209 days stays almost constant around 1. In Figure 15, the [O I] / [Ca II] ratio of CCSNe (from Kuncarayakti et al. 2015) is plotted, where SN 2017iro is shown with a star symbol. It indicates that the progenitor of SN 2017iro is comparatively a less massive star in a binary system. A less massive progenitor in a binary system has been proposed in several Type Ib SNe such as SN 2007Y (Stritzinger et al. 2009), and iPTF13bvn (Bersten et al. 2014; Eldridge et al. 2015; Kuncarayakti et al. 2015). This is in agreement with the fact that binary interaction is a favored scenario in a majority ($\geqslant$70%) of massive stars (Podsiadlowski et al. 1992; Sana et al. 2012).

The nucleosynthesis calculations for zero-age sequence progenitor masses of 13, 15, 20, and 25 $M_\odot$ were performed by Thielemann et al. (1996), and the corresponding oxygen masses were estimated as 0.22, 0.43, 1.48, and 3.00 $M_\odot$, respectively. Limongi & Chieffi (2003) also computed explosive yields of massive stars in the mass range 13–35 $M_\odot$ with an initial solar composition using the FRANEC (Chieffi et al. 1998) code. Their estimated oxygen mass is $\sim$0.3 and $\sim$0.5 $M_\odot$ for 13 and 15 $M_\odot$ progenitor masses, respectively. Both the nucleosynthesis calculations indicate that the estimated oxygen mass of 0.35 $M_\odot$ could be produced by a progenitor star with zero-age main-sequence mass in the

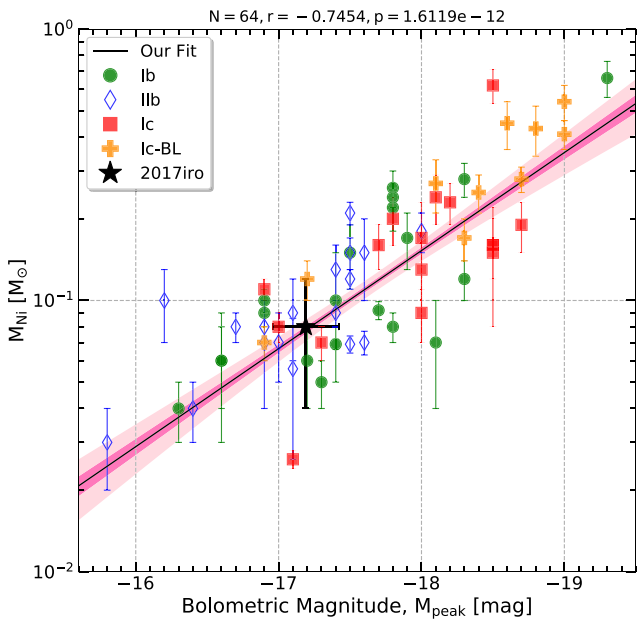

Figure 14. Correlation between M_{bol} and ^{56}Ni mass of 47 SE-SNe (including the sample from Lyman et al. 2016 and nine additional events; see Section 5.3). Types Ib, Ic, Ic-BL, and IIb are shown with different symbols. The thick solid line is the best fit. The dark-pink and light-pink shaded regions are indicative of 1σ and 3σ confidence intervals of the fit, respectively.

Table 7
In Addition to Lyman et al. (2016), the Following Events Are Used to Estimate Correlation between M_{bol} and ^{56}Ni Mass (see Section 5.3)

Name	Type	M_{bol} (mag)	^{56}Ni Mass ($M_\odot$)	References
SN 2011ei	IIb	−15.8	0.03 ± 0.01	1
SN 2011fu	IIb	−17.5	0.21 ± 0.02	2
SN 2012ap	Ic-BL	−17.2	0.12 ± 0.02	3
SN 2012au	Ib	−17.8	0.26 ± 0.04	4, 5, 6
SN 2013df	IIb	−16.2	0.10 ± 0.03	7, 8
SN 2014ad	Ic-BL	−18.1	0.27 ± 0.06	9
SN 2015as	IIb	−16.7	0.08 ± 0.01	10
SN 2016coi	Ic/Ic-BL[a]	−16.9	0.11 ± 0.01	11
SN 2016gkg	IIb	−17.4	0.09 ± 0.01	12

References. (1) Milisavljevic et al. (2013a); (2) Kumar et al. (2013); (3) Milisavljevic et al. (2015); (4) Milisavljevic et al. (2013b); (5) Pandey et al. (2021); (6) Takaki et al. (2013); (7) Morales-Garoffolo et al. (2014); (8) Szalai et al. (2016); (9) Sahu et al. (2018); (10) Gangopadhyay et al. (2018); (11) Kumar et al. (2018;); (12) Tartaglia et al. (2017).
[a] Ic/Ic-BL transitional event.

Table 8
Oxygen Mass of Type Ib SNe

Name	Oxygen Mass ($M_\odot$)	References
SN 1996N	0.11–0.21	1
SN 2007Y	0.20	2
SN 2009jf	1.34	3
iPTF13bvn	0.33	4
MOT[a]	0.90	5
SN 2017iro	0.35	This study

Note.
[a] Master OT J120451.50+265946.6
References. (1) Sollerman et al. (1998); (2) Stritzinger et al. (2009); (3) Sahu et al. (2011); (4) Kuncarayakti et al. (2015); (5) Singh et al. (2019).

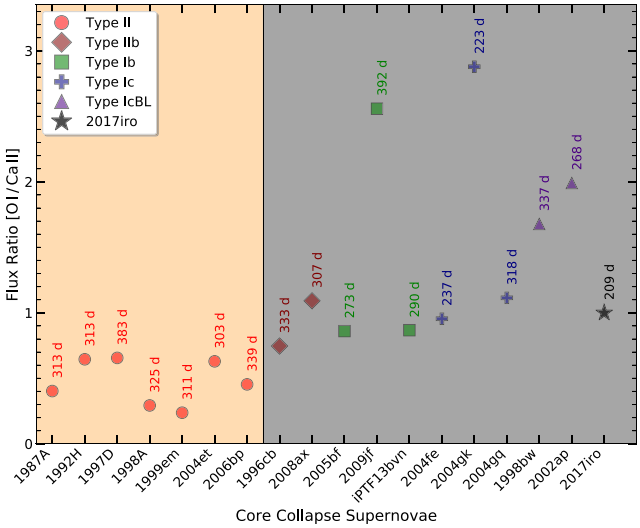

Figure 15. [O I] λλ6300, 6364 / [Ca II] λλ7291, 7324 line ratio of CCSNe from Kuncarayakti et al. (2015). The [O I]/[Ca II] ratio for SN 2017iro obtained from the nebular spectra (between +173 and +209 days) has been shown with a star symbol. The phases (relative to the time of maximum light) are shown next to the each data point. The left (orange) and right (gray) regions belong to Type II and SE-SNe, respectively. The references for spectra are the following: SN 1987A (Pun et al. 1995), SN 1992H (Clocchiatti et al. 1996), SN 1997D (Benetti et al. 2001), SN 1998A (Pastorello et al. 2005), SN 1998bw (Patat et al. 2001), SN 1999em (Leonard et al. 2002), SN 2004et (Sahu et al. 2006), SN 2004gq (Maeda et al. 2008), SN 2005bf (Maeda et al. 2007b), SN 2006bp (Quimby et al. 2007), SN 1996cb, SN 2002ap, SN 2004fe, SN 2004gk, SN 2008ax, and SN 2009jf (Modjaz et al. 2008, 2014).

range ∼13–15 $M_\odot$. It is further supported by the findings of Fang et al. (2019), where the upper limit of the Type IIb/Ib SN progenitors is proposed as ∼17 $M_\odot$ for a progenitor in a binary system (see also Taddia et al. 2018; Prentice et al. 2019). It is worth mentioning that the estimated oxygen mass for SN 2017iro (Section 5.3.2) is only a lower limit of the total oxygen mass. With the increased uncertainty range (0.28–1.05 $M_\odot$), the range of possible progenitor masses increases substantially, especially toward the higher progenitor masses (∼20 $M_\odot$). However, the lower value of the [O I] / [Ca II] ratio indicates a lower zero-age main-sequence mass progenitor of SN 2017iro.

The pre-explosion images of NGC 5480 available in the HST archive (observed on 2017 January 17, Proposal ID: 14840, PI: Andrea Bellini), were examined to identify the possible progenitor candidate of SN 2017iro. The image was obtained with ACS/WFC in filter F606W. A diffuse source with an extent of 5 pixels was detected in the pre-explosion images at the SN location. At the adopted distance of the host galaxy, the extent corresponds to ∼35 pc. This extended source could possibly be a star cluster hosting the progenitor of SN 2017iro.

6. Summary

We have presented optical photometric (40 epochs) and spectroscopic (34 epochs) follow-up of the Type Ib SN 2017iro. The LC evolution in *UBVRI* follows the usual trend of SE-SNe, i.e., blue passbands peak before the red passbands, indicating that the SN photosphere is rapidly cooling. The Δm_{15} parameters (for *BVRI* bands) are comparable to those estimated for a large SE-SNe sample (Drout et al. 2011; Taddia et al. 2018)

and in particular to SN 2012au. Further, the colors of SN 2017iro evolve similarly to Type Ib events. The absolute V-band and bolometric ($\log_{10} L$) luminosities are -17.76 mag and 42.39 erg s^{-1}, respectively, indicative of a moderately luminous SN. The explosion parameters were computed by applying different analytical models to the quasi-bolometric LCs, which yield a ^{56}Ni mass of $\sim$0.05–0.10 $M_{\odot}$, $M_{\rm ej}$ of $\sim$1.4–4.3 $M_{\odot}$, and $E_k \sim$ (0.8–1.9) $\times$ 10^{51} erg.

There seem to be two groups of Type Ib SNe in terms of the LC tail decline rates, suggesting a heterogeneity (Wheeler et al. 2015) in the late-time LC evolution. However, lack of an adequate amount of data during the late phase of these events could be a possible reason for such inference. Hence, late-phase monitoring of a larger sample of such events may provide a clearer insight to this finding. The late-phase LCs of SN 2017iro decayed with moderate steepness, indicating incomplete γ-ray trapping by the SN ejecta. A low to moderate level of ^{56}Ni mixing is supported by the nonmonotonic evolution of color curves (Dessart et al. 2012; Yoon et al. 2019) in the case of SN 2017iro. However, we cannot draw a firm conclusion owing to unavailability of sufficient early-phase data of this event.

In the first optical spectrum (-7 days) of SN 2017iro, the He I λ5876 feature is clearly identified. Other He I lines such as $\lambda\lambda$4471, 6678, and 7065 are comparatively weak in the beginning, but they never became as strong as He I λ5876. The ejecta velocity estimated using the Fe II λ5169 line is $\sim$9000 km s^{-1} near B-band maximum, which became almost constant at $\sim$5500 km s^{-1} beyond +25 days. The Mg I] line is very weak during the nebular phase in SN 2017iro. The general spectroscopic behavior of SN 2017iro is similar to that of SN 2009jf and iPTF13bvn. The metallicity near the SN 2017iro location (12 + log (O/H) = 8.64) is similar to the solar value. A neutral oxygen mass of $\sim$0.35 $M_{\odot}$ was estimated in the ejecta. The [O I] / [Ca II] line ratio observed in SN 2017iro indicates that the progenitor had a main-sequence mass of $\sim$13–15 $M_{\odot}$. The inferred neutral oxygen mass and the progenitor main-sequence mass for SN 2017iro are very similar to the Type Ib SN iPTF13bvn that occurred in a binary system.

We thank the referee for critical review and constructive suggestions that helped to improve the paper. We also thank Sung-Chul Yoon and Hanindyo Kuncarayakti for sharing the data. B.K., D.K.S., and G.C.A. acknowledge BRICS grant DST/IMRCD/BRICS/PilotCall1/MuMeSTU/2017(G) for the present work. D.K.S. and G.C.A. also acknowledge DST/JSPS grant DST/INT/JSPS/P/281/2018. We are grateful to the observers at HCT who provided their valuable time to monitor this event and also thank the staff of IAO, Hanle, and CREST, Hosakote, that made these observations possible. The Weizmann interactive supernova data repository (WISeREP; http://wiserep.weizmann.ac.il) is also acknowledged. This research has made use of the NASA/IPAC Extragalactic Database (NED), which is operated by the Jet Propulsion Laboratory, California Institute of Technology, under contract with the National Aeronautics and Space Administration. This research made use of REDPIPE[5] (Singh 2021), an assemblage of data reduction and analysis scripts written by AS.

[5] https://github.com/sPaMFouR/RedPipe

ORCID iDs

Brajesh Kumar https://orcid.org/0000-0001-7225-2475
Avinash Singh https://orcid.org/0000-0003-2091-622X
D. K. Sahu https://orcid.org/0000-0002-6688-0800
G. C. Anupama https://orcid.org/0000-0003-3533-7183

References

Anderson, J. P. 2019, A&A, 628, A7
Anderson, J. P., Habergham, S. M., James, P. A., & Hamuy, M. 2012, MNRAS, 424, 1372
Arcavi, I., Gal-Yam, A., Yaron, O., et al. 2011, ApJL, 742, L18
Arcavi, I., Hosseinzadeh, G., Brown, P. J., et al. 2017, ApJL, 837, L2
Arnett, W. D. 1982, ApJ, 253, 785
Asplund, M., Grevesse, N., Sauval, A. J., & Scott, P. 2009, ARA&A, 47, 481
Barbon, R., Benetti, S., Cappellaro, E., et al. 1995, A&AS, 110, 513
Barbon, R., Benetti, S., Cappellaro, E., Rosino, L., & Turatto, M. 1990, A&A, 237, 79
Benetti, S., Turatto, M., Balberg, S., et al. 2001, MNRAS, 322, 361
Benetti, S., Turatto, M., Valenti, S., et al. 2011, MNRAS, 411, 2726
Bersten, M. C., Benvenuto, O. G., Folatelli, G., et al. 2014, AJ, 148, 68
Bersten, M. C., Tanaka, M., Tominaga, N., Benvenuto, O. G., & Nomoto, K. 2013, ApJ, 767, 143
Bertrand, E. 2017, Transient Name Server Classification Report, 2017-1555
Bianco, F. B., Modjaz, M., Hicken, M., et al. 2014, ApJS, 213, 19
Cano, Z. 2013, MNRAS, 434, 1098
Cano, Z., Maeda, K., & Schulze, S. 2014, MNRAS, 438, 2924
Cao, Y., Kasliwal, M. M., Arcavi, I., et al. 2013, ApJL, 775, L7
Cardelli, J. A., Clayton, G. C., & Mathis, J. S. 1989, ApJ, 345, 245
Chieffi, A., Limongi, M., & Straniero, O. 1998, ApJ, 502, 737
Chugai, N. N. 2000, AstL, 26, 797
Clocchiatti, A., Benetti, S., Wheeler, J. C., et al. 1996, AJ, 111, 1286
Clocchiatti, A., & Wheeler, J. C. 1997, ApJ, 491, 375
Conti, P. S. 1975, MSRSL, 9, 193
Couch, S. M., Pooley, D., Wheeler, J. C., & Milosavljević, M. 2011, ApJ, 727, 104
Crowther, P. A. 2007, ARA&A, 45, 177
Dessart, L., & Hillier, D. J. 2005, A&A, 439, 671
Dessart, L., Hillier, D. J., Li, C., & Woosley, S. 2012, MNRAS, 424, 2139
Dessart, L., Hillier, D. J., Woosley, S., et al. 2015, MNRAS, 453, 2189
Dessart, L., Hillier, D. J., Woosley, S., et al. 2016, MNRAS, 458, 1618
Drout, M. R., Soderberg, A. M., Gal-Yam, A., et al. 2011, ApJ, 741, 97
Eldridge, J. J., Fraser, M., Maund, J. R., & Smartt, S. J. 2015, MNRAS, 446, 2689
Eldridge, J. J., Fraser, M., Smartt, S. J., Maund, J. R., & Crockett, R. M. 2013, MNRAS, 436, 774
Elmhamdi, A. 2011, AcA, 61, 179
Elmhamdi, A., Danziger, I. J., Cappellaro, E., et al. 2004, A&A, 426, 963
Ensman, L. M., & Woosley, S. E. 1988, ApJ, 333, 754
Fang, Q., Maeda, K., Kuncarayakti, H., Sun, F., & Gal-Yam, A. 2019, NatAs, 3, 434
Filippenko, A. V. 1988, AJ, 96, 1941
Filippenko, A. V. 1997, ARA&A, 35, 309
Filippenko, A. V., Matheson, T., & Ho, L. C. 1993, ApJL, 415, L103
Folatelli, G., Van Dyk, S. D., Kuncarayakti, H., et al. 2016, ApJL, 825, L22
Foley, R. J., Papenkova, M. S., Swift, B. J., et al. 2003, PASP, 115, 1220
Fransson, C., & Chevalier, R. A. 1989, ApJ, 343, 323
Fremling, C., Sollerman, J., Taddia, F., et al. 2014, A&A, 565, A114
Fremling, C., Sollerman, J., Taddia, F., et al. 2016, A&A, 593, A68
Galbany, L., Stanishev, V., Mourão, A. M., et al. 2016, A&A, 591, A48
Gal-Yam, A. 2017, in Handbook of Supernovae, ed. A. W. Alsabti & P. Murdin (Cham: Springer)
Gangopadhyay, A., Misra, K., Pastorello, A., et al. 2018, MNRAS, 476, 3611
Graur, O., Bianco, F. B., Huang, S., et al. 2017a, ApJ, 837, 120
Graur, O., Bianco, F. B., Modjaz, M., et al. 2017b, ApJ, 837, 121
Groh, J. H., Georgy, C., & Ekström, S. 2013, A&A, 558, L1
Hachisu, I., Matsuda, T., Nomoto, K., & Shigeyama, T. 1991, ApJL, 368, L27
Hamuy, M., Maza, J., Pinto, P. A., et al. 2002, AJ, 124, 417
Harkness, R. P., Wheeler, J. C., Margon, B., et al. 1987, ApJ, 317, 355
Heger, A., Fryer, C. L., Woosley, S. E., Langer, N., & Hartmann, D. H. 2003, ApJ, 591, 288
Kamble, A., Soderberg, A. M., Chomiuk, L., et al. 2014, ApJ, 797, 2
Kilpatrick, C. D., Drout, M. R., Auchettl, K., et al. 2021, MNRAS, 504, 2073

Kilpatrick, C. D., Foley, R. J., Abramson, L. E., et al. 2017, MNRAS, 465, 4650
Kilpatrick, C. D., Takaro, T., Foley, R. J., et al. 2018, MNRAS, 480, 2072
Kumar, B., Pandey, S. B., Sahu, D. K., et al. 2013, MNRAS, 431, 308
Kumar, B., Singh, A., Srivastav, S., Sahu, D. K., & Anupama, G. C. 2018, MNRAS, 473, 3776
Kuncarayakti, H., Maeda, K., Bersten, M. C., et al. 2015, A&A, 579, A95
Landolt, A. U. 1992, AJ, 104, 340
Leibundgut, B., Kirshner, R. P., Pinto, P. A., et al. 1991, ApJ, 372, 531
Leonard, D. C., Filippenko, A. V., Gates, E. L., et al. 2002, PASP, 114, 35
Li, W., Leaman, J., Chornock, R., et al. 2011, MNRAS, 412, 1441
Limongi, M., & Chieffi, A. 2003, ApJ, 592, 404
Liu, Y.-Q., Modjaz, M., Bianco, F. B., & Graur, O. 2016, ApJ, 827, 90
Lucy, L. B. 1991, ApJ, 383, 308
Lyman, J. D., Bersier, D., James, P. A., et al. 2016, MNRAS, 457, 328
Maeda, K., Kawabata, K., Mazzali, P. A., et al. 2008, Sci, 319, 1220
Maeda, K., Kawabata, K., Tanaka, M., et al. 2007a, ApJL, 658, L5
Maeda, K., Mazzali, P. A., & Nomoto, K. 2006, ApJ, 645, 1331
Maeda, K., Tanaka, M., Nomoto, K., et al. 2007b, ApJ, 666, 1069
Malesani, D., Fynbo, J. P. U., Hjorth, J., et al. 2009, ApJL, 692, L84
Massey, P. 2003, ARA&A, 41, 15
Maund, J. R., Fraser, M., Ergon, M., et al. 2011, ApJL, 739, L37
Maund, J. R., Smartt, S. J., Kudritzki, R. P., Podsiadlowski, P., & Gilmore, G. F. 2004, Natur, 427, 129
Maund, J. R., Wheeler, J. C., Baade, D., et al. 2009, ApJ, 705, 1139
Mazzali, P. A., Kawabata, K. S., Maeda, K., et al. 2005, Sci, 308, 1284
Mazzali, P. A., Valenti, S., Della Valle, M., et al. 2008, Sci, 321, 1185
Milisavljevic, D., Fesen, R. A., Gerardy, C. L., Kirshner, R. P., & Challis, P. 2010, ApJ, 709, 1343
Milisavljevic, D., Margutti, R., Parrent, J. T., et al. 2015, ApJ, 799, 51
Milisavljevic, D., Margutti, R., Soderberg, A. M., et al. 2013a, ApJ, 767, 71
Milisavljevic, D., Patnaude, D. J., Chevalier, R. A., et al. 2018, ApJL, 864, L36
Milisavljevic, D., Soderberg, A. M., Margutti, R., et al. 2013b, ApJL, 770, L38
Minkowski, R. 1941, PASP, 53, 224
Modjaz, M., Blondin, S., Kirshner, R. P., et al. 2014, AJ, 147, 99
Modjaz, M., Gutiérrez, C. P., & Arcavi, I. 2019, NatAs, 3, 717
Modjaz, M., Kewley, L., Bloom, J. S., et al. 2011, ApJL, 731, L4
Modjaz, M., Kirshner, R. P., Blondin, S., Challis, P., & Matheson, T. 2008, ApJL, 687, L9
Modjaz, M., Li, W., Butler, N., et al. 2009, ApJ, 702, 226
Morales-Garoffolo, A., Elias-Rosa, N., Benetti, S., et al. 2014, MNRAS, 445, 1647
Morales-Garoffolo, A., Elias-Rosa, N., Bersten, M., et al. 2015, MNRAS, 454, 95
Mould, J. R., Huchra, J. P., Freedman, W. L., et al. 2000, ApJ, 529, 786
Nadyozhin, D. K. 1994, ApJS, 92, 527
Nicholl, M. 2018, RNAAS, 2, 230
Nomoto, K. 1984, ApJ, 277, 791
Nomoto, K. 1987, ApJ, 322, 206
Nomoto, K. I., Iwamoto, K., & Suzuki, T. 1995, PhR, 256, 173
Pandey, S. B., Kumar, A., Kumar, B., et al. 2021, MNRAS, 507, 1229
Pastorello, A., Baron, E., Branch, D., et al. 2005, MNRAS, 360, 950
Pastorello, A., Kasliwal, M. M., Crockett, R. M., et al. 2008, MNRAS, 389, 955
Patat, F., Cappellaro, E., Danziger, J., et al. 2001, ApJ, 555, 900
Pauldrach, A. W. A., Vanbeveren, D., & Hoffmann, T. L. 2012, A&A, 538, A75
Perlmutter, S., Pennypacker, C., Graham, J. R., & Soifer, B. T. 1988, IAU Circ., 4590, 1
Pettini, M., & Pagel, B. E. J. 2004, MNRAS, 348, L59
Phillips, M. M. 1993, ApJL, 413, L105
Phillips, M. M., Simon, J. D., Morrell, N., et al. 2013, ApJ, 779, 38
Piro, A. L., & Nakar, E. 2013, ApJ, 769, 67
Podsiadlowski, P., Joss, P. C., & Hsu, J. J. L. 1992, ApJ, 391, 246
Podsiadlowski, P., Langer, N., Poelarends, A. J. T., et al. 2004, ApJ, 612, 1044
Pols, O. R., & Dewi, J. D. M. 2002, PASA, 19, 233
Poznanski, D., Ganeshalingam, M., Silverman, J. M., & Filippenko, A. V. 2011, MNRAS, 415, L81
Poznanski, D., Prochaska, J. X., & Bloom, J. S. 2012, MNRAS, 426, 1465
Prabhu, T. P. 2014, PINSA, 80, 887
Prentice, S. J., Ashall, C., James, P. A., et al. 2019, MNRAS, 485, 1559
Prentice, S. J., Mazzali, P. A., Pian, E., et al. 2016, MNRAS, 458, 2973
Puls, J., Vink, J. S., & Najarro, F. 2008, A&ARv, 16, 209
Pun, C. S. J., Kirshner, R. P., Sonneborn, G., et al. 1995, ApJS, 99, 223
Quimby, R. M., Wheeler, J. C., Höflich, P., et al. 2007, ApJ, 666, 1093
Richardson, D., Branch, D., & Baron, E. 2006, AJ, 131, 2233
Richmond, M. W., Treffers, R. R., Filippenko, A. V., et al. 1994, AJ, 107, 1022
Roming, P. W. A., Pritchard, T. A., Brown, P. J., et al. 2009, ApJL, 704, L118
Roy, R., Kumar, B., Maund, J. R., et al. 2013, MNRAS, 434, 2032
Ryder, S. D., Van Dyk, S. D., Fox, O. D., et al. 2018, ApJ, 856, 83
Sahu, D. K., Anupama, G. C., Chakradhari, N. K., et al. 2018, MNRAS, 475, 2591
Sahu, D. K., Anupama, G. C., Srividya, S., & Muneer, S. 2006, MNRAS, 372, 1315
Sahu, D. K., Gurugubelli, U. K., Anupama, G. C., & Nomoto, K. 2011, MNRAS, 413, 2583
Sana, H., de Mink, S. E., de Koter, A., et al. 2012, Sci, 337, 444
Sánchez, S. F., Kennicutt, R. C., Gil de Paz, A., et al. 2012, A&A, 538, A8
Sanders, N. E., Soderberg, A. M., Levesque, E. M., et al. 2012, ApJ, 758, 132
Schlafly, E. F., & Finkbeiner, D. P. 2011, ApJ, 737, 103
Schlafly, E. F., Meisner, A. M., Stutz, A. M., et al. 2016, ApJ, 821, 78
Schlegel, E. M., & Kirshner, R. P. 1989, AJ, 98, 577
Shahbandeh, M., Hsiao, E. Y., Ashall, C., et al. 2022, ApJ, 925, 175
Shigeyama, T., Nomoto, K., Tsujimoto, T., & Hashimoto, M.-A. 1990, ApJL, 361, L23
Shivvers, I., Filippenko, A. V., Silverman, J. M., et al. 2019, MNRAS, 482, 1545
Singh, A. 2021, RedPipe: Reduction Pipeline, Astrophysics Source Code Library, ascl:2106.024
Singh, M., Misra, K., Sahu, D. K., et al. 2019, MNRAS, 485, 5438
Smartt, S. J. 2009, ARA&A, 47, 63
Smith, N. 2006, ApJ, 644, 1151
Smith, N. 2014, ARA&A, 52, 487
Smith, N., & Owocki, S. P. 2006, ApJL, 645, L45
Soderberg, A. M., Berger, E., Page, K. L., et al. 2008, Natur, 453, 469
Sollerman, J., Leibundgut, B., & Spyromilio, J. 1998, A&A, 337, 207
Srivastav, S., Anupama, G. C., & Sahu, D. K. 2014, MNRAS, 445, 1932
Stalin, C. S., Hegde, M., Sahu, D. K., et al. 2008, BASI, 36, 111
Stritzinger, M., Hamuy, M., Suntzeff, N. B., et al. 2002, AJ, 124, 2100
Stritzinger, M., & Leibundgut, B. 2005, A&A, 431, 423
Stritzinger, M., Mazzali, P., Phillips, M. M., et al. 2009, ApJ, 696, 713
Stritzinger, M. D., Taddia, F., Burns, C. R., et al. 2018, A&A, 609, A135
Stritzinger, M. D., Taddia, F., Holmbo, S., et al. 2020, A&A, 634, A21
Sutherland, P. G., & Wheeler, J. C. 1984, ApJ, 280, 282
Swartz, D. A. 1991, ApJ, 373, 604
Szalai, T., Vinkó, J., Nagy, A. P., et al. 2016, MNRAS, 460, 1500
Taddia, F., Sollerman, J., Leloudas, G., et al. 2015, A&A, 574, A60
Taddia, F., Stritzinger, M. D., Bersten, M., et al. 2018, A&A, 609, A136
Takaki, K., Kawabata, K. S., Yamanaka, M., et al. 2013, ApJL, 772, L17
Takáts, K., & Vinkó, J. 2012, MNRAS, 419, 2783
Tartaglia, L., Fraser, M., Sand, D. J., et al. 2017, ApJL, 836, L12
Taubenberger, S., Valenti, S., Benetti, S., et al. 2009, MNRAS, 397, 677
Theureau, G., Hanski, M. O., Coudreau, N., Hallet, N., & Martin, J. M. 2007, A&A, 465, 71
Thielemann, F.-K., Nomoto, K., & Hashimoto, M.-A. 1996, ApJ, 460, 408
Toy, V. L., Cenko, S. B., Silverman, J. M., et al. 2016, ApJ, 818, 79
Turatto, M., Benetti, S., & Cappellaro, E. 2003, in Proc. ESO-MPA-MPE Workshop, From Twilight to Highlight: The Physics of Supernovae, ed. W. Hillebrandt & B. Leibundgut (Berlin: Springer), 200
Uomoto, A. 1986, ApJL, 310, L35
Vacca, W. D., & Leibundgut, B. 1996, ApJL, 471, L37
Valenti, S., Benetti, S., Cappellaro, E., et al. 2008, MNRAS, 383, 1485
Valenti, S., Fraser, M., Benetti, S., et al. 2011, MNRAS, 416, 3138
Van Dyk, S. D., Zheng, W., Brink, T. G., et al. 2018, ApJ, 860, 90
Van Dyk, S. D., Zheng, W., Clubb, K. I., et al. 2013, ApJL, 772, L32
Vinkó, J., Blake, R. M., Sárneczky, K., et al. 2004, A&A, 427, 453
Wellstein, S., & Langer, N. 1999, A&A, 350, 148
Wellstein, S., Langer, N., & Braun, H. 2001, A&A, 369, 939
Wheeler, J. C., Johnson, V., & Clocchiatti, A. 2015, MNRAS, 450, 1295
Wheeler, J. C., & Levreault, R. 1985, ApJL, 294, L17
Wiggins, P. 2017, Transient Name Server Discovery Report, No. 2017-1354
Williamson, M., Modjaz, M., & Bianco, F. B. 2019, ApJL, 880, L22
Woosley, S. E., & Eastman, R. G. 1997, in NATO Advanced Science Institutes (ASI) Ser. C, 486, Thermonuclear Supernovae, ed. P. Ruiz-Lapuente, R. Canal, & J. Isern (Dordrecht: Kluwer), 821
Woosley, S. E., Langer, N., & Weaver, T. A. 1995, ApJ, 448, 315
Woosley, S. E., & Weaver, T. A. 1995, ApJS, 101, 181
Xiang, D., Wang, X., Mo, J., et al. 2019, ApJ, 871, 176
Yoon, S.-C. 2015, PASA, 32, e015
Yoon, S.-C., Chun, W., Tolstov, A., Blinnikov, S., & Dessart, L. 2019, ApJ, 872, 174
Yoon, S.-C., Woosley, S. E., & Langer, N. 2010, ApJ, 725, 940